UNIVERSIDADE FEDERAL DO CEARÁ

CENTRO DE TECNOLOGIA

DEPARTAMENTO DE ENGENHARIA METALÚRGICA E DE MATERIAIS

PROGRAMA DE PÓS-GRADUAÇÃO EM ENGENHARIA E CIÊNCIA DE MATERIAIS

RAQUELE LIMA MOREIRA

ELECTRICAL AND CHARGE TRANSPORT PROPERTIES OF ZnO-BASED TRANSPARENT CONDUCTIVE ELECTRODES FOR OPTOELECTRONICS

FORTALEZA

2024

RAQUELE LIMA MOREIRA

ELECTRICAL AND CHARGE TRANSPORT PROPERTIES OF ZnO-BASED TRANSPARENT CONDUCTIVE ELECTRODES FOR OPTOELECTRONICS

Doctoral Thesis submitted to the Post-Graduate Program in Materials Science and Engineering of the Federal Univer- sity of Ceará in partial fulfillment of the requirements for the degree of Doctor in Materials Science and Engineering. Concentration area: Physical and Mechanical Properties of Materials.

Supervisor: Prof. Dr. Igor Frota de Vasconcelos.

FORTALEZA

2024

Dados Internacionais de Catalogação na Publicação
Universidade Federal do Ceará
Sistema de Bibliotecas
Gerada automaticamente pelo módulo Catalog, mediante os dados fornecidos pelo(a) autor(a)

M839e Moreira, Raquele Lima.
Electrical and charge transport properties of ZnO-based transparent conductive electrodes for optoelectronics. / Raquele Lima Moreira. – 2023.
72 f. : il. color.

Tese (doutorado) – Universidade Federal do Ceará, Centro de Tecnologia, Programa de Pós-Graduação em Engenharia e Ciência de Materiais, Fortaleza, 2023.
Orientação: Prof. Dr. Igor Frota de Vasconcelos.

1. Zinc oxide. 2. Transparent electrodes. 3. Grain boundaries. I. Título.

CDD 620.11

RAQUELE LIMA MOREIRA

ELECTRICAL AND CHARGE TRANSPORT PROPERTIES OF ZnO-BASED TRANSPARENT CONDUCTIVE ELECTRODES FOR OPTOELECTRONICS

Doctoral Thesis submitted to the Post-Graduate Program in Materials Science and Engineering of the Federal Univer- sity of Ceará in partial fulfillment of the requirements for the degree of Doctor in Materials Science and Engineering. Concentration area: Physical and Mechanical Properties of Materials.

Approval date: 01/April/2024

THESIS COMMITTEE

Prof. Dr. Igor Frota de Vasconcelos (Supervisor)
Universidade Federal do Ceará (UFC)

Prof. Dr. Francisco Eroni Paz dos Santos Universidade Federal do Piauí (UFPI)

Prof. Dr. Francisco Carlos Carneiro Soares Salomão
Universidade Estadual do Ceará (UECE)

Prof. Dr. Eduardo Bedê Barros
Universidade Federal do Ceará (UFC)

Prof. Dr. Luis Paulo Mourão dos Santos Universidade Federal do Ceará (UFC)

This thesis is dedicated to all students and researchers who are seriously committed to research and the dissemination of knowledge.

ACKNOWLEDGEMENTS

I want to thank all the professors and technicians of the Postgraduate Program in Engineering and Materials Science at the Federal University of Ceará for sharing your expertise in the world of materials. Special thanks to colleagues Luis Paulo Santos, Jorge Luís, Samuel Lucas, Nádia Aline, Carlos Salomão, and, most especially, to my supervisor, Prof. Igor Frota de Vasconcelos, for all their help and collaboration in the preparation of this thesis and their commitment to science. I would also like to thank the thesis committee for the time dedicated to analyzing and correcting the content covered here and Prof. Eduardo Bede Barros, coordinator of the Advanced Microscopy Laboratory of the Physics Department, for making available the atomic force microscope without which this thesis it would not be possible. And to my research colleagues at the Advanced Materials Laboratory, I want to express my sincere thanks for their daily company and patience.

This study was financed in part by the Coordenação de Aperfeiçoamento de Pessoal de Nível Superior – Brasil (CAPES) – Finance Code 001.

ABSTRACT

The present study systematically explored the structure and charge transport characteristics at the junction between a platinum-iridium (Pt-Ir) metal tip and transparent zinc oxide (ZnO) electrodes of varying film thicknesses. ZnO nanoparticles were synthesized through the coprecipitation method and dispersed in dichlorobenzene. Characterization of the nanoparticles involved X-ray diffraction, Raman spectroscopy, and UV-vis spectroscopy. The ZnO dispersions were spin- coated onto a conductive substrate to produce films comprising one, four, and eight layers. To investigate the films' nanoscale surface electrical properties and charge transport mechanisms, electrostatic force microscopy (EFM), Kelvin probe force microscopy (KPFM), and conducting atomic force microscopy (c-AFM) techniques were employed. The study examined the influence of grain boundaries (GBs) and thickness on films' electrical and optoelectronic properties. Variations in film thickness resulted in changes in the metal-semiconductor (M-S) contact type, transitioning from ohmic to rectifying with increasing layers. The modulation in the M-S contact type was primarily attributed to the presence of GBs during film formation. EFM measurements indicated charge trapping within the GB region, suggesting localized band-bending effects. KPFM measurements revealed slightly higher local work function values in the GB region across all samples, attributed to Fermi level shifts towards the conduction band induced by optically active states introduced by GBs. For single-layer films, semiconductor work functions exceeded those of the metal, suggesting the formation of ohmic contacts with no potential barrier to transport, as per Mott and Schottky theory. In contrast, four and eight-layer films exhibited lower work function values than the metal and thus typical rectifying behavior akin to Schottky diodes, governed by thermionic emission theory. The study underscored the influence of grain boundaries and film thickness on the optoelectronic and charge transport properties of conductive and transparent ZnO electrodes, emphasizing its significance in forming versatile M-S contacts crucial for diverse semiconductor applications.

Keywords: zinc oxide; transparent electrodes; grain boundaries.

RESUMO

O presente estudo explorou sistematicamente a estrutura e as características de transporte de carga na junção entre um contato metálico Pt-Ir e eletrodos transparentes de óxido de zinco (ZnO) com diferentes espessuras de filme. Nanopartículas de ZnO foram sintetizadas pelo método de coprecipitação e dispersas em diclorobenzeno. A caracterização das nanopartículas envolveu difração de raios-X, espectroscopia Raman e espectroscopia UV-vis. As dispersões de ZnO foram depositadas em um substrato condutor para produzir filmes com uma, quatro e oito camadas. Para investigar as propriedades elétricas e os mecanismos de transporte de carga em nanoescala da superfície dos filmes, foram empregadas técnicas de microscopia de força eletrostática (EFM), microscopia de força de sonda Kelvin (KPFM) e microscopia de força atômica condutora (c-AFM). O estudo examinou a influência dos contornos de grão (GBs) e da espessura nas propriedades elétricas e optoeletrônicas dos filmes. Variações na espessura do filme resultaram em mudanças no tipo de contato metal-semicondutor (MS), passando de ôhmico para retificador com o aumento das camadas. A modulação no tipo de contato MS foi atribuída principalmente à presença de GBs durante a formação do filme. As medidas de EFM indicaram aprisionamento de carga na região de GB, sugerindo efeitos localizados de curvatura de banda. As medições KPFM revelaram valores de função de trabalho local ligeiramente mais elevados na região GB em todas as amostras, atribuídos a mudanças no nível de Fermi em direção à banda de condução induzida por estados opticamente ativos introduzidos por GBs. Para filmes de camada única, as funções trabalho do semicondutor excederam as do metal, sugerindo a formação de contatos ôhmicos sem barreira de potencial ao transporte, conforme a teoria de Mott e Schottky. Em contraste, os filmes de quatro e oito camadas exibiram valores de função trabalho mais baixos do que o metal e, portanto, um comportamento retificador típico semelhante aos diodos Schottky, governados pela teoria da emissão termiônica. O estudo ressaltou a influência dos contornos de grão e da espessura dos filmes nas propriedades optoeletrônicas e de transporte de carga de eletrodos de ZnO condutores e transparentes, enfatizando sua importância na formação de contatos MS versáteis, cruciais para diversas aplicações de semicondutores.

Palavras-chave: óxido de zinco; eletrodos transparentes; contornos de grão.

LIST OF FIGURES

LIST OF TABLES

CONTENTS

1 INTRODUCTION AND OBJECTIVES

Thin film transparent electrodes are essential in most optoelectronic, photonic, and next-generation photovoltaic devices, all experiencing increasing demand. Thin film technology has been emerging and replacing many components previously manufactured in what we can call a solid state or from materials that, due to their specificities, make manufacturing processes more expensive and make their access and dissemination difficult. It is, therefore, a technology that has been making processes cheaper, consuming less energy in its stages and being able to give your devices faster reactions and responses, as is the case with thin film transistors (TFTs), a type of transistor field effect formed by a layer of metallic semiconductor oxide on an insulating substrate, often used in the form of an integrated system in display applications, such as liquid crystal displays (LCDs). An LCD screen includes a transistor for each pixel, which means the current that drives the pixel's lighting can be smaller and turn on and off more quickly. They are on cell phones, notebooks, televisions, and other widely circulated devices.

In addition to transistors, third-generation solar cells may be completely manufactured by superimposing films from the front and rear electrodes to the active layers (1). Varistors (2), a type of resistor with variable resistance according to the potential difference applied between its terminals, which are commonly used as part of circuits protecting current or voltage surges, have already been manufactured in the form of a thin film on rigid and flexible substrates.

Like any emerging technology, thin-film devices also have limitations, such as poor color accuracy or fluctuation in image quality in the case of TFTs or lower power conversion efficiencies in the case of solar cells. However, these are acceptable challenges given the main objective of modern society, which is energy conservation, with the aim of minimizing greenhouse gas emissions to guarantee a better future for future generations.

In this sense, many researchers are engaged in the search for new processes and, mainly, new materials such as transition metal oxides which, due to their excellent optoelectronic properties, such as a wide bandgap, optical transparency, and high charge mobility, have been applied as interfacial layers for transporting electrons or holes, maintaining operating stability under ambient conditions, and being compatible, in terms of energy level alignment, with other semiconductor oxides (3).

Among several possible transition metal oxides, zinc oxide stands out for its ease, numerous manufacturing possibilities, and optical, electrical, and charge transport properties.

Zinc oxide is a semiconductor with a wide and direct band gap of approximately 3.37 eV at room temperature and an excitonic binding energy of around 60 meV (4). It can form highly transparent thin films within the visible region of the solar spectrum. When undoped, ZnO typically exhibits n-type conductivity, stemming from intrinsic defects like interstitial Zn and oxygen vacancies, and showcases a broad range of work functions, spanning from approximately
3.0 eV to over 5.0 eV (5, 6). The low work function values allow for favorable alignment with the work function of transparent conductive oxides (TCOs) commonly found in electrodes, such as FTO (approximately 4.4 eV), facilitating electron injection and hole blocking in the same direction (7).

It is common for grain boundaries (GB) to appear when synthesizing ZnO films or pellets. This happens due to the thermodynamic forces that act during the formation of films on substrates, or due to the high pressures and temperatures of pellet synthesis. Grain boundaries are regions that introduce crystal defects (in addition to defects characteristic of the material itself) that induce local band bending at the grain face/grain boundary junction, creating potential barriers that can influence conduction processes at the interface. This effect is controlled in order to favor the properties of the device in which they are present. In solar cells, for example, grain boundaries can limit the passage of current due to the potential barrier formed when, in fact, you want more current to pass, as a solar cell works to generate energy. In the case of varistors, the higher the potential barrier, the better their operation, as these devices control voltage surges that could damage the elements of the circuit into which they are integrated.

Another interesting feature of ZnO-based structures is that ZnO thin films can establish ohmic or Schottky contacts with metals, depending on film synthesis parameters, such as annealing temperature, deposition technique, and film thickness (8), which in turn influence the formation of GBs. Many ZnO-based devices necessitate electrodes with robust ohmic contacts, as low contact resistance, insignificant compared to the bulk resistance of the semiconductor, can lead to a lower voltage drop across the electrode, thus enhancing the current injection efficiency of the device (9, 10). Reyes et al. (11) demonstrated current gain, albeit at slower response speeds, using ohmic contacts in photoconductive-type photodetectors. Conversely, photodetectors with Schottky contact electrodes generally exhibited faster response speeds and less noise current, as Su et al. (12) reported. Hwang and Hong (13) observed that a significant Schottky-barrier height (SBH) at the metal-semiconductor interface of Schottky-barrier photodetectors leads to a small leakage current and high breakdown voltage, thereby enhancing device performance.

Nanoscale devices must precisely control band bending to form appropriate contacts for each application. In most semiconductors, band-bending effects primarily occur due to the presence of GBs. These boundaries, characterized by high concentrations of structural defects, disrupt the crystal lattice

and act as electron traps, creating defect states below the conduction band. Consequently, these defects influence the charge transport mechanisms through materials. It is in this sense that this thesis sought to exhaustively investigate, using mainly electrostatic force microscopy (EFM), Kelvin probe force microscopy (KPFM), and conductive atomic force microscopy (c-AFM) techniques, how the defect states introduced by the presence of grain boundaries influence the electrical and optoelectronic properties of ZnO thin films deposited on conductive FTO substrates, widely applied as transparent electrodes in optoelectronic devices. In an additional way, the study examined the influence of film thickness on the formation of ohmic and rectifying contacts. Along with electrical measurements, the films underwent spectroscopic analysis to reveal their optical and structural characteristics.

1.1 Effect of grain boundaries on the physical properties of a semiconductor

Figure 1a shows a schematic of the energy band diagram of a semiconductor, characterized by an interval between the conduction and valence bands, called a bandgap. As with n-type semiconductors, the Fermi level is close to the conduction band. The work function and electron affinity can also be observed, defined in relation to the vacuum level.

The work function is defined as the amount of energy required to raise an electron from the Fermi level to the vacuum level, which is the energy level of an electron outside the material with zero kinetic energy, calculated by the difference between the levels, being, therefore, a measure of the potential barrier that electrons must overcome to leave the material. It is an extremely important parameter in the electronic emission process required in photoelectronics. The electronic affinity, defined as the interval between the vacuum level and the bottom of the conduction band, and the bandgap, characteristic parameters of the semiconductor, should not be variable values (despite the quantum confinement effects associated with particle sizes). particles that can lead to the blue or redshift of the absorption edges characteristic of the material and, consequently, the change in value in its bandgap). The work function is a parameter that varies with the doping level or with the presence of defect states, both introduced at the Fermi level, which causes the Fermi level to shift towards the conduction band, approaching each other, consequently reducing the value of their work function, as shown in Fig. 1 (right side).

Figure 1 – Energy band diagram scheme of a semiconductor, highlighting physical properties (left) and defect states introduced on Fermi level on grain boundary region (right).

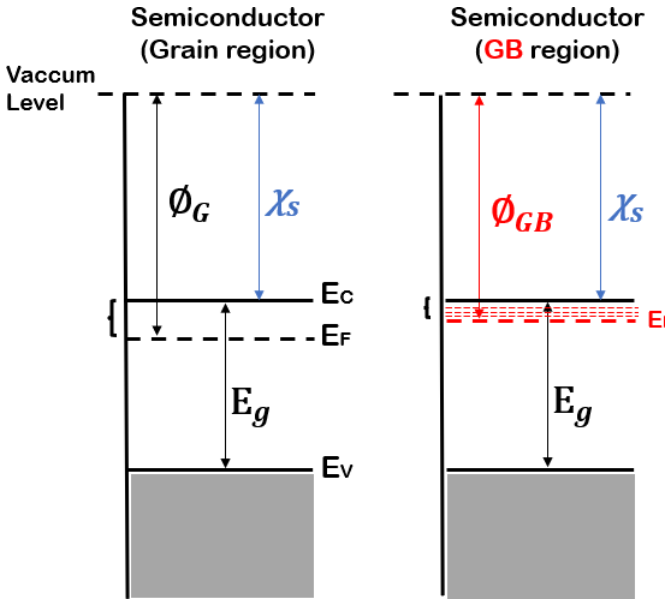

Source: Author.

Since the close contact between a metal and a semiconductor leads to Fermi level alignment until equilibrium is reached, the displacement of the semiconductor's Fermi level, caused by the defect states introduced by GBs, should influence the formation of a greater or lesser potential barrier at the M-S interface and, therefore, in the formation of an ohmic contact or rectifier.

1.2 Formation of ohmic and rectifiers M-S contacts and associated charge transport mechanisms

According to the Schottky-Mott theory (14, 15), when dealing with an n-type semi-conductor with $\Phi_M < \Phi_S$ (where Φ_M and Φ_S are the metal and semiconductor work functions), the metal-semiconductor contact exhibits non-rectifying behavior, indicating the formation of an ohmic contact.

In the case where the work function of the semiconductor is greater than the work function of the metal (as seen in Fig. 2a), the electrons on the metal are at a higher energy level when the materials are brought into contact (Fig. 2b), electrons begin to flow from the metal to the semiconductor conduction band until the Fermi levels (E_F) are aligned. As electrons migrate from the metal to the semiconductor, the concentration of free electrons in the semiconductor region near the boundary increases, while positive charges remain on the metal side. The charge

accumulation layer in the semiconductor is confined to a thickness on the order of the Debye length, essentially forming a surface charge. Due to the high concentration of electrons in the metal, positive charges are also superficial and are contained at a distance of about 0.5 Å from the metal-semiconductor interface. Consequently, there is no formation of a depletion region in the semiconductor, nor a potential barrier for the flow of electrons, either from the semiconductor towards the metal or in the opposite direction (10).

Figure 2 – Energy band diagram of the local M-S contact with Φm < Φs at the grain and grain boundary regions: (a) before contact, (b) in thermal equilibrium and (c) thermionic process.

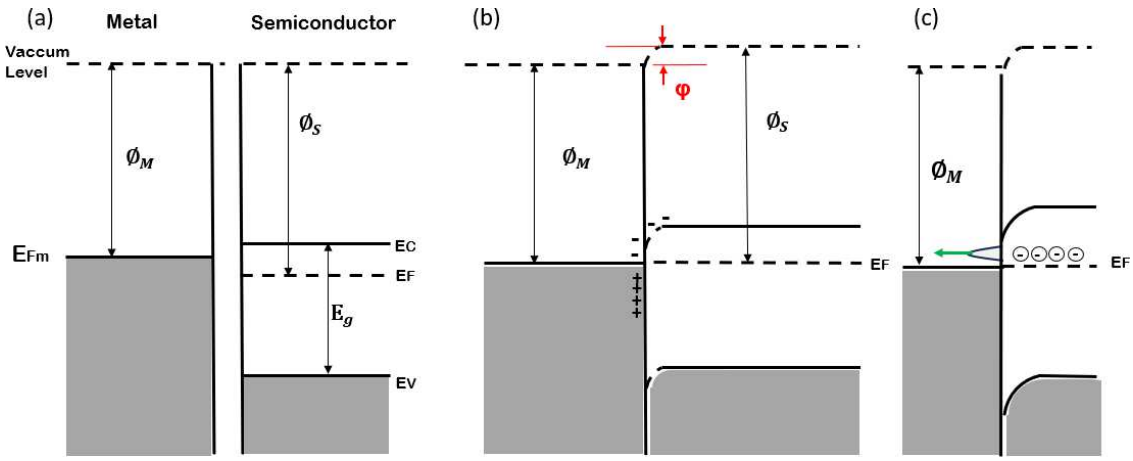

Source: Author.

Furthermore, as the number of electrons in the semiconductor increases, the distance between E_F and the edge of the conduction band (E_C) decreases. However, in thermal equilibrium, E_F remains constant, causing E_C to shift upward parallel to the edge of the valence band (E_V) and the vacuum level. This shift occurs because the semiconductor's optical band gap and electron affinity, defined as the energy difference of an electron between the vacuum level and the lower edge of the conduction band, remain unchanged after contact with the metal.

In a metal-semiconductor system in thermal equilibrium, the vacuum level must maintain continuity through the transition region. Consequently, to ensure continuity, the vacuum level on the semiconductor side must gradually approach the vacuum level on the metal side, resulting in band bending (ϕ). The difference in vacuum levels, equivalent to the difference in work functions, determines the local band curvature (16). Due to the thin depletion region formed, electrons with energy close to the Fermi level can tunnel from the semiconductor into the metal at low temperatures in a field emission transport process (10) (as illustrated in Fig. 2c). These processes can explain the electron transport through the M-S ohmic contact observed.

In the case where the work function of the semiconductor is smaller than the work function of the metal (when $\Phi_M > \Phi_S$), the metal-semiconductor contact exhibits rectifying behavior, indicating the formation of a potential barrier. Upon bringing the semiconductor into contact with the metal tip, the electrons from the semiconductor's conduction band, which have higher energy than those in the metal (Fig. 3a and b), flow into the metal until the Fermi levels align. As electrons transfer from the semiconductor to the metal, the concentration of free electrons near the interface diminishes, leading to a displacement of E_F away from the conduction band edge E_C.

Figure 3 – Energy band diagram of the local M-S contact with Φm > Φs at the grain and grain boundary regions: (a) before contact, (b) in thermal equilibrium and (c) thermionic process.

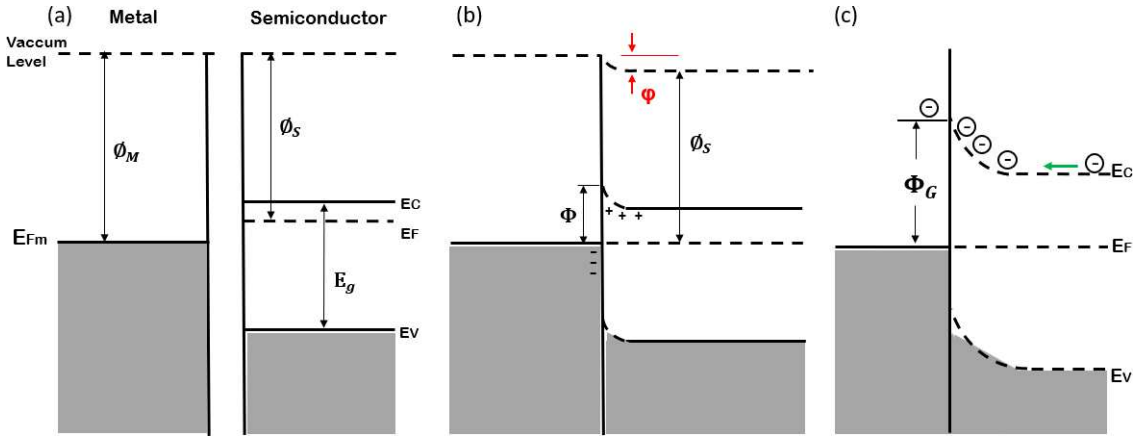

Source: Author.

In thermal equilibrium, E_F remains constant, causing E_C to shift upward. The gap and electron affinity must remain unchanged after contact, as mentioned, and E_V also shifts upward in parallel with E_C along with the vacuum level, which gradually approaches the vacuum level on the metal side, to maintain continuity in the transition region, resulting in band bending. In a Schottky barrier diode, current flows due to charge transport from the semiconductor to the metal or in the reverse direction. An electron emitted over the barrier from the semiconductor into the metal must traverse the high-field depletion region. While traversing this region, drift and diffusion processes govern the electron's motion. However, in the thermionic emission theory, the effect of drift and diffusion in the depletion region is negligible, and the barrier height is assumed to be large compared to k_BT. Therefore, only those electrons whose kinetic energy exceeds the height of the potential barrier (as illustrated in Fig. 3c) can reach the top and move toward the metal.

The formation of a potential barrier at the M-S interface indicates that charge transport predominantly occurs through thermionic emission. The thermionic emission model equations allow for calculating potential barrier height values and saturation currents. According to it, the current through the junction barrier as a function of the applied voltage is given by (17, 18):

$$I = I^S \exp\left(-\frac{qV}{nk_BT}\right) - 1 \ , \tag{1.1}$$

where the saturation current I^S depends on the potential barrier according to:

$$I^S \propto \exp\left(-\frac{\Phi}{nk_BT}\right) \ , \tag{1.2}$$

where Φ is the Schottky barrier height (SBH), n is the ideality factor, k_B is the Boltzmann constant and, T is the temperature. According to the TE model, the Schottky diode parameters n and Φ are presumed independent of voltage. These parameters are derived, respectively, from the slope and intercept of the line that best fits the relationship between $\ln I$ and V, expressed as:

$$\ln I = \frac{qV}{nk_BT} + \ln I^S. \tag{1.3}$$

Considering the presence of GBs, with both grain and GB forming similar contacts, it possible to calculate the change in potential barrier height $\Delta\Phi$ can be calculated as:

$$\Delta\Phi = nk_BT \ln\left(\frac{I^S_{\mathrm{G}}}{I^S_{\mathrm{GB}}}\right) \ , \tag{1.4}$$

where I^S_{G} and I^S_{GB} are the saturation currents at the grain and the grain boundary (19).

The ohmic and rectifying behaviors can be inferred from the behavior of the IV curves. Ohmic behavior can be observed in linear I-V curves, where the resistance of the bulk semiconductor region determines the current and is independent of the direction of applied polarization. The slope of the straight portion in curve IV can provide the overall resistance value (as shown in Fig. 4a). A rectifier contact (Fig 4b) will exhibit the characteristic behavior of a diode, where the current only starts to be conducted when it reaches a certain forward bias voltage (which, in the case of Schottky-type diodes, is in the order of 0.3 to 0.5V – values smaller than pn junction diodes).

Figure 4 – IV curve behavior of M-S contact: (a) ohmic and (b) rectifier type.

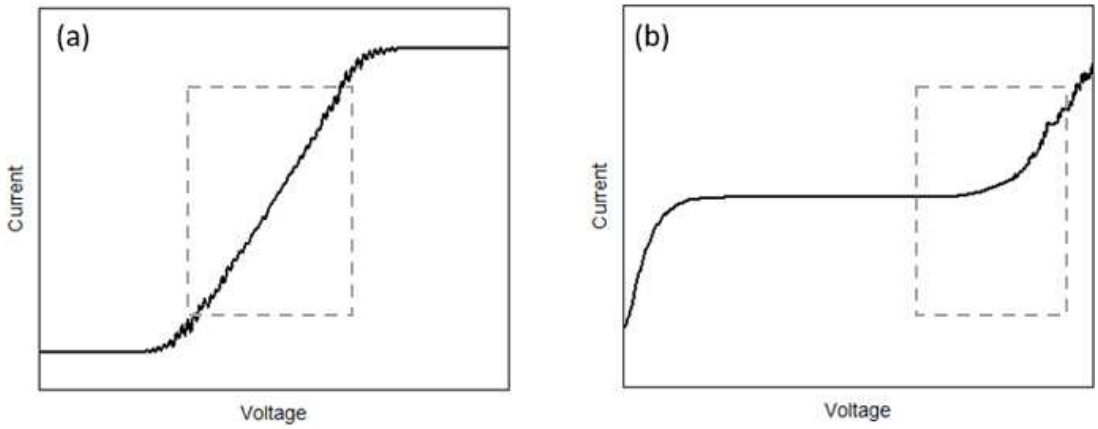

Source: Author.

1.3 Methodology applied to identify the existence and influence of grain boundaries on electrical and charge transport properties in ZnO films

The morphology and surface roughness of all synthesized ZnO films were assessed through AFM scans. EFM measurements were conducted to scan surface topography, with the aim to evidence the charge trapping in GB regions and, consequently, to confirm the presence of defect states that shift the Fermi level of the semiconductor toward the conduction band. KPFM measurements were employed to derive local work function values and confirm the formation of an ohmic or rectifying metal-semiconductor contact. Ohmic and rectifying behaviors were documented in IV curves obtained via c-AFM. The Thermionic emission (TE) model equations provided insights into the charge transport of Schottky barrier devices, extracting local saturation current and local potential barrier height data. Additionally, ultraviolet-visible (UV- vis) spectroscopy was utilized to ascertain the optical properties of the films. X-ray diffraction (XRD) and Raman spectroscopy (just in the samples of Chapter 1) were employed to analyze their structural properties.

1.4 Objectives

The primary goal of this study is to thoroughly examine the impact of defect states resulting from grain boundaries on the charge transport characteristics of transparent electrodes composed of thin zinc oxide films deposited on a conductive substrate for optoelectronic applica- tions. To accomplish this goal, the following specific objectives have been delineated:

- Synthesize zinc oxide nanoparticles via coprecipitation, followed by the deposition of the films onto a transparent conductive substrate using the spin coating technique.
- Obtain samples with varying film thicknesses (one, four, and eight layers) to evaluate the impact of thickness as a control parameter on the formation of diverse metal-semiconductor contacts and subsequent charge transport properties.
- Analyze the optical properties of the films using ultraviolet-visible (UV-vis) spectroscopy.
- Investigate the structural properties of the films through X-ray diffraction (XRD) and Raman spectroscopy.
- Determine the local electrical properties utilizing EFM, KPFM, and c-AFM modes of atomic force microscopy.
- Establish potential correlations between optical and structural properties with the local electrical properties to enhance our understanding of the charge transport mechanism through the electrodes.

1.5 Outline

This thesis is structured in an alternative format for dissertations and theses, which allows the doctoral candidate to insert scientific articles authored by the candidate in chapters.

Chapter 1 provided the theoretical basis necessary to analyze and understand the results presented in the following chapters. Therefore, the reader can observe the repetition of information throughout the chapters regarding the sample preparation procedure and the theory dealing with the formation of ohmic and rectifying contacts between metal and semiconductors.

Chapter 2 - Influence of Grain Boundaries on Nanoscale Charge Transport Properties of Transparent Conductive ZnO-based Electrode: published on **ACS Applied Electronic Materials**, 2024, 6, 1, 415–425, https://doi.org/10.1021/acsaelm.3c01423.

Chapter 3 - Ohmic-to-Schottky Modification of ZnO-Metal Contact Modulated by Film Thickness: to be submitted to a scientific journal.

Chapter 4 - Conclusions and Future Work.

2 INFLUENCE OF GRAIN BOUNDARIES ON NANOSCALE CHARGE TRANSPORT PROPERTIES OF TRANSPARENT CONDUCTIVE ZnO-BASED ELECTRODE

The presence of defect states, such as grain boundaries (GB), can interfere with the charge transport properties of various semiconductor oxides. In this research, electrostatic force microscopy (EFM) and conducting atomic force microscopy (c-AFM) techniques were used to explore the nanoscale surface electrical properties of zinc oxide (ZnO) thin films deposited on a conductive fluorine-doped tin oxide (FTO) substrate. Films like these are often used as anode materials in photovoltaic and other optoelectronic devices. EFM measurements revealed the presence of charge trapping within the grain boundary region, suggesting localized band-bending effects. Furthermore, a current map obtained through c-AFM indicated that the grain regions exhibited higher conductivity, validating the observations made with EFM. By combining c-AFM and Kelvin probe force microscopy (KPFM), it was possible to obtain experimental confirmation of band bending at grain boundaries. Data extracted from current-voltage (I-V) curves allowed the quantification of local saturation currents of 1.29 nA and 0.75 nA at the grain and GB. It was also possible to calculate the difference in potential barrier height between grain and GB as 50.40 meV. Urbach energy calculations identified the existence of defect states within the band gap. These defect states shifted the Fermi level towards the conduction band, reducing the local work functions to 3.93 eV and 3.89 eV for the grain and GB. These findings align with the thermionic emission model (TE) and Schottky-Mott theory, contributing to a deeper understanding of nanoscale charge transport within ZnO-based anodes, and paving the way for the development of transparent conductive oxide-based optoelectronic devices and other applications.

2.1 Introduction

Transition metal oxides (TMO) have gained significant importance as thin film materials in photovoltaic and in several other optoelectronic devices due to their noteworthy optical and electrical properties like a wide bandgap (E_g), optical transparency, and robust charge mobility (19). In contrast to inorganic semiconductor-based devices where surface doping facilitates ohmic contacts, applications employing TMO-based transparent conductive electrodes require meticulous interface engineering to establish ohmic contacts, enabling efficient charge transport and extraction (20, 3, 21, 22). Achieving proper ohmic contacts has been realized by employing TMO as interfacial layers, transporting holes or electrons to the metal contacts while maintaining stability under ambient conditions, visible light transparency, and proper band alignment with an array of semiconductors (23).

Among TMO, zinc oxide is the most frequently employed electron transport layer (24, 25, 26). ZnO is categorized as an n-type semiconductor due to inherent crystalline defects like oxygen vacancies and interstitial Zn atoms. It boasts a wide direct bandgap (approximately 3.37 eV at room temperature) and exhibits the capacity to form thin films with high optical transparency and electronic mobility (27, 28, 29, 30). Furthermore, ZnO thin films exhibit a wide range of work functions, spanning from around 3.0 eV to over 5.0 eV (5, 6). The low work function values enable favorable alignment with the work function of transparent conductive oxides (TCO), typically found in the front electrodes of devices (e.g., approximately 4.4 eV for FTO). This alignment facilitates electron injection and hole blocking in the same direction (7).

ZnO thin films are easily processable via solution-based methods, including the sol-gel route (31) and ZnO colloidal techniques (32). This versatility allows film formation using common substrate-coating methods like spin coating and roll-to-roll printing. Most film growth techniques involve local nanoparticle agglomeration and the formation of GB, influenced by thermodynamic driving forces (33).

It is well-documented that grain boundaries significantly impact the electronic prop- erties of many semiconductors. These regions introduce numerous crystalline defects that induce local band bending at the grain face/grain boundary junction, creating potential barriers that can influence the conduction processes at the interface. These defects can also be charge traps, leading to recombination processes and reduced device efficiency. Consequently, characteristics such as spatial charge distribution, grain size, structure, and the nature of GB in films play pivotal roles in dictating device performance (34, 35).

The presence of GB can also enhance device performance, as demonstrated by independent studies (36, 37). They reported solar cells with $CuIn_{1-x}Ga_xSe_2$ (CIGSe) absorber layers that achieved exceptional conversion efficiencies ($> 20\%$) despite the prevalence of GB.
The improved efficiency was attributed to collecting minority carriers in the grain boundary region. Conversely, in the case of ZnO thin film transistors, potential barriers formed at GB are considered the primary limiting factor for device performance (38). Higher potential barriers result in more significant band bending upon contact with the metal, potentially hindering charge transport across the metal-semiconductor interface. Therefore, understanding the nature and dimension of potential barriers, local band bending, and charge transport across the film surface is essential to optimizing high-performance devices.

The investigation of local band bending in pure and doped ZnO thin films has been done through direct and indirect methods. For instance, Likovich *et al.*(39), utilizing scanning tunneling microscopy (STM), demonstrated that the accumulation of traps in GB of Al-doped ZnO (AZO) films created a distribution of defect states below the conduction band ($\sim$ 100 meV), affecting electron transport properties. Bikowski e Ellmer(40) studied the relationship between electronic transport and structural properties in AZO films, associating GB defects with Al dopants. However,

they lacked direct microscopic evidence of local band bending in GB regions.

Information on band bending in GB, local charge transport, and interfacial band alignment across heterojunctions has also been obtained from scanning probe microscopy modes such as c-AFM, EFM, and KPFM (41). Kumar *et al.*(17) demonstrated the formation of potential barriers at the GB of AZO films. Furthermore, using c-AFM, these researchers revealed that the local band bending measured in the GB region resulted from the defect-induced electrostatic potential barrier and polarization-driven barrier. Sharma *et al.*(42) illustrated the formation of potential barriers in ZnO films using KPFM, finding a heterogeneous work function distribution along the film surface. This electronic properties variation, attributed to surface crystallinity variations, can significantly influence interfacial charge transport. Singh e Som(19) demonstrated charge trapping at grain boundaries of $ZnO:SnO_2$ (ZTO: zinc-tin oxide) films using both c-AFM and EFM measurements, suggesting the existence of local band bending.

This study aims to elucidate the difference in potential barrier heights between grains and GB and the consequential band bending that modulates and influences the local charge transport process in ZnO thin films. Scanning probe microscopy in c-AFM, EFM, and KPFM modes was employed to investigate these aspects. Before electrical measurements, the films were subjected to spectroscopic analyses to unveil their optical and structural characteristics. These characterizations confirmed the formation of ZnO in its most stable structure, possessing a characteristic optical gap consistent with the semiconductor. They also unveiled the presence of defect states correlating with the formation of grain boundaries, as indicated by Urbach energy calculations. Using c-AFM and EFM, the current distribution on the surface was mapped, providing evidence of charge trapping at GB. For nanoscale charge transport analyses in grains and GB, local I-V measurements were conducted with c-AFM, enabling the calculation of the difference in potential barrier height between grains and GB. Since the work function is an intrinsic surface property that characterizes the potential barrier formed, KPFM measurements were performed to gain insights into lateral variations of the work function and its distribution on the film surface. The work function values corroborated the formation of a metal-semiconductor rectifying contact and the emergence of a larger potential barrier at GB, resulting in higher local band bending in that region. This study paves the way for developing transparent conductive oxide-based electrodes for optoelectronic devices and other TMO-based applications.

2.2 Experimental procedure

In this study, all reagents employed were utilized without any additional purification. Nanoscale electrical measurements were conducted using the atomic force microscopy modes c-AFM, EFM, and KPFM. To gain deeper insights into the physical characteristics and establish potential correlations with the local electrical properties, all synthesized films were subjected to analysis through

x-ray diffraction (XRD), ultraviolet-visible (UV-vis) absorption spectroscopy, and Raman spectroscopy. The methods are described below, and a schematic representation of the experimental procedure is shown in Fig. 5.

2.2.1 Synthesis of ZnO nanoparticles and depositions of films

Zinc oxide nanoparticles were synthesized from the hydrolysis and condensation of zinc acetate dihydrate ($Zn(CH_3COO)_2 \cdot 2H_2O$, Neon) using potassium hydroxide (KOH, Sigma Aldrich) in absolute methanol (CH_3OH, Sigma-Aldrich) at a Zn^{2+}:OH^- molar ratio of 1:2. This synthesis method was adapted from previous studies conducted independently (32, 43, 44).

The procedure involved the following steps: $Zn(CH_3COO)_2 \cdot 2H_2O$ (2.97 g) was dissolved in methanol (125 ml) and heated to 60°C. Separately, KOH (1.51 g) was dissolved in methanol (65 ml) and heated to 60°C. This KOH solution was added to the zinc acetate solution over 30 seconds, making the mixture cloudy. The mixture was continuously stirred and gently refluxed at the same temperature for 3 hours. The mixture was left to stand at room temperature for 24 hours. The mixture was carefully decanted, and the precipitate was re-suspended in methanol (125 ml). It was allowed to settle for an additional 24 hours. The methanol was removed, ensuring the precipitate was drained without completely drying.

Figure 5 – Schematic representation of the experimental procedure. Step 1: synthesis of ZnO nanoparticles; Step 2: dispersion of NP in dichlorobenzene; Step 3: film deposition on FTO by spin coating; Step 4: thermal treatment of film; Step 5: electrical characterization.

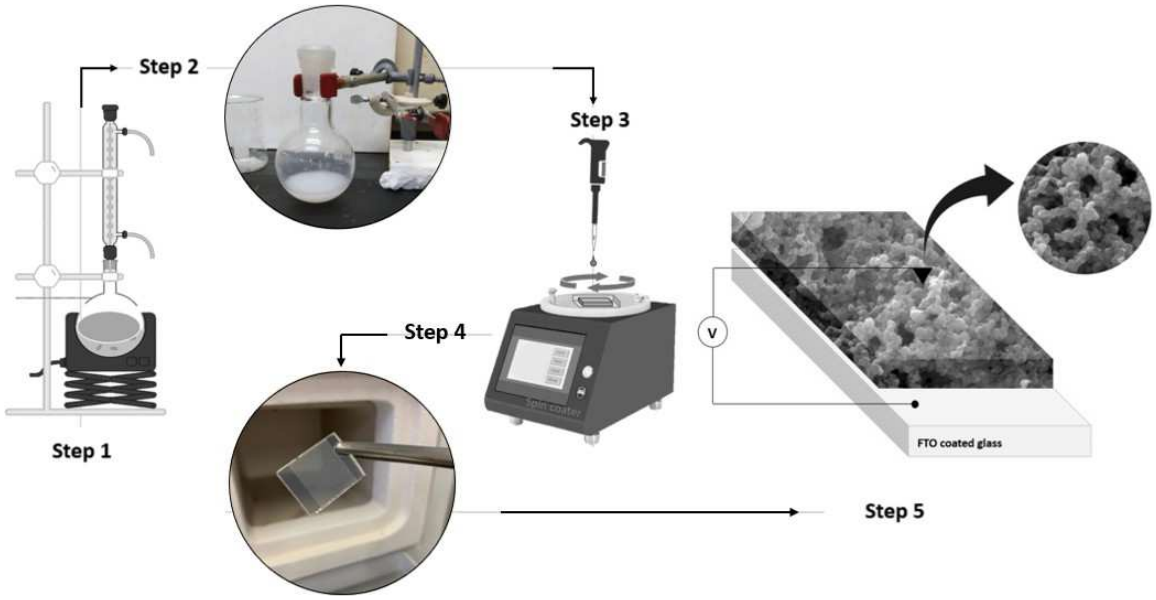

Source: Author.

The precipitated ZnO nanoparticles, insoluble in pure methanol, were redispersed in anhydrous 1,2-dichlorobenzene (Sigma Aldrich) at 50 mg/ml. To maintain nanoparticle stability in the solution, 2-(2-methoxyethoxy)acetic acid, MEAA (Sigma Aldrich), was added at a concentration of 4% w/w relative to ZnO. These dispersions exhibited a cloudy whitish appearance.

TCO substrates consisting of FTO-coated glass with a surface resistivity of approximately 7 Ω/sq and dimensions of 20 mm × 10 mm × 2.5 mm (Sigma Aldrich) were used as the substrate material. The FTO substrates underwent a thorough cleaning process, which included a 15-minute ultrasonic cleaning with a detergent solution, deionized water, and isopropyl alcohol. Next, a 50 mg/ml zinc oxide solution, stabilized with 4% w/w MEAA, was spin-coated onto the FTO substrates using a vacuum-free Ossila spin coater at 1200 rpm for 30 seconds. Subsequently, the substrate was heated on a hot plate at 310°C for 5 minutes to polymerize the zinc oxide film, rendering it insoluble (32). This deposition process, followed by thermal treatment, was repeated four times. Finally, all samples underwent a 30-minute thermal treatment under the same conditions.

2.2.2 Characterization techniques

Transmittance spectra were collected at room temperature using a UV-Vis spectrophotometer, specifically the Shimadzu model UV-2600, equipped with an integrating sphere (ISR-2600Plus). The measurements covered the wavelength range of 220 to 800 nm.

For Raman spectroscopy, an Alpha 300 Witec system was employed. The excitation source was the 532 nm laser line, delivering a laser power of 0.6 mW to the sample, and an accumulation time of 2 seconds was used.

X-ray diffraction patterns of the samples were recorded using a Rigaku SmartLab SE X-ray diffractometer. This instrument featured a theta-theta goniometer configured in Bragg- Brentano geometry and operated at a power of 1.4 W (40 kV and 35 mA). The radiation source utilized was CoKα ($\lambda = 0.1789$ nm), and the scan ranged from 20° to 80° in 2θ.

All nanoscale electrical measurements were carried out using an atomic force micro- scope, specifically the Asylum MFP-3D-Bio AFM from Oxford Instruments. Conductive tips (Pointprobe Silicon SPM-Sensor probes, NanoWorld) were used, featuring a tip radius of 20 nm, stiffness of 2.8 Nm^{-1}, resonant frequency of 75 kHz, and platinum-iridium (Pt-Ir) coating.

c-AFM measurements were performed in contact mode. For KPFM and EFM measurements, elevation mode was used, maintaining a height of 40 nm above the film surface. Local I-V measurements were conducted with the Pt-Ir conductive tip and the FTO substrate configured as the top and bottom electrodes, respectively. This configuration formed a Pt- Ir/ZnO/FTO heterojunction through which electron transport occurred.

These measurements were conducted at numerous selected locations, with scan speeds varying from 0.2 to 0.5 Hz, across three samples prepared under identical conditions.

2.3 Results and discussion

2.3.1 Structural and optical properties

Figure 6a displays the x-ray diffraction pattern of the ZnO thin film deposited on the FTO conductive substrate. The XRD pattern of FTO exhibits distinct diffraction peaks, including {110}, {101}, {200}, and {211}, which correspond to the planes of polycrystalline SnO_2 and are consistent with the tetragonal rutile crystalline structure (space group P42/mnm), as confirmed by ICSD catalog number 9163.

For reference, a typical catalog sheet of the wurtzite-type hexagonal crystalline structure of ZnO (ICSD 26170) was included in the experimental diffraction pattern. It reveals a peak at $2\theta = 40.19^{\circ}$, corresponding to the {002} family of planes characteristic of ZnO. Consequently, the {002} basal planes of ZnO overlap with the {101} planes of SnO_2:F. However, it's worth noting that the experimental peak positions differ from the ICSD standard, possibly due to variations in the lattice parameters of the material (45). Some expected peaks couldn't be identified due to their low intensity, posing a challenge in distinguishing them from the low signal-to-noise ratio of the background. Additionally, the peak with low intensity observed around $2\theta = 35^{\circ}$ was not indexed in either of the crystal structures and remains unidentified.

Furthermore, the sharp peak widths observed may suggest the formation of a non-homogeneous film, comprised of densely packed grains consisting of numerous nanoparticles with different crystallinity (46).

Figure 6b shows the UV-Vis transmittance spectrum of a ZnO film on FTO substrate. The noticeable drop in transmittance at approximately 380 nm is attributed to the fundamental absorption edge of ZnO (47). The transmittance, as per the Beer-Lambert law (Eq. 2.1), is an optical property that is heavily dependent on the film thickness (48):

$$-\log I(\lambda)/I_0(\lambda) = -\log T(\lambda) \equiv A(\lambda) = c\varepsilon(\lambda)t, \tag{2.1}$$

where $I(\lambda)$ and $I_0(\lambda)$ are the intensities of the incident and transmitted radiation at the wavelength λ, $A(\lambda)$ is the absorbance, c is the volumetric molar concentration of the absorptive species, $\varepsilon(\lambda)$ is the molar absorption coefficient of the material, and t is the film thickness. An increase in thickness indicates an extended optical path length, leading to greater light absorption and, consequently, a decrease in the detected transmission signal. In the case of the fabricated films, the accumulation of layers resulted in increased film thickness, causing a reduction in transmittance to approximately

75% within the visible region. Apart from the thickness effect, the rise in photon scattering due to the formation of defects, such as oxygen vacancies, also contributes to the decrease in the average transmittance of the films in the visible region (49).

The points of inflection of the transmission spectrum, identified as the maxima in the first derivative, can be interpreted as indicative of the absorption edges (50, 51). Consequently, the energy bandgaps were calculated by identifying the peaks in the first derivative of the UV-Vis spectrum, as illustrated in the inset of Fig. 6. The peak at 3.75 eV is attributed to the FTO substrate as its optical band gap falls within 3.6 to 4.0 eV, depending on the level of fluorine incorporation (52). The other peak is assigned to the absorption by the ZnO film. The bandgap of 3.33 eV is aligned with previously reported values for bulk ZnO (30, 53) and ZnO thin films (54, 55). The average ZnO particle size was determined by TEM to be about 50 nm. At this size range, quantum confinement effects are not expected to influence the gap (56, 57).

Figure 6 – (a) X-ray diffraction patterns of ZnO film on FTO substrate; (b) UV-vis transmittance spectrum (inset: 1st derivative showing the absorption of FTO and ZnO); (c) Urbach energy plot for a ZnO film; (d) Raman spectra of the FTO substrate, and ZnO films deposited on FTO and Si substrates.

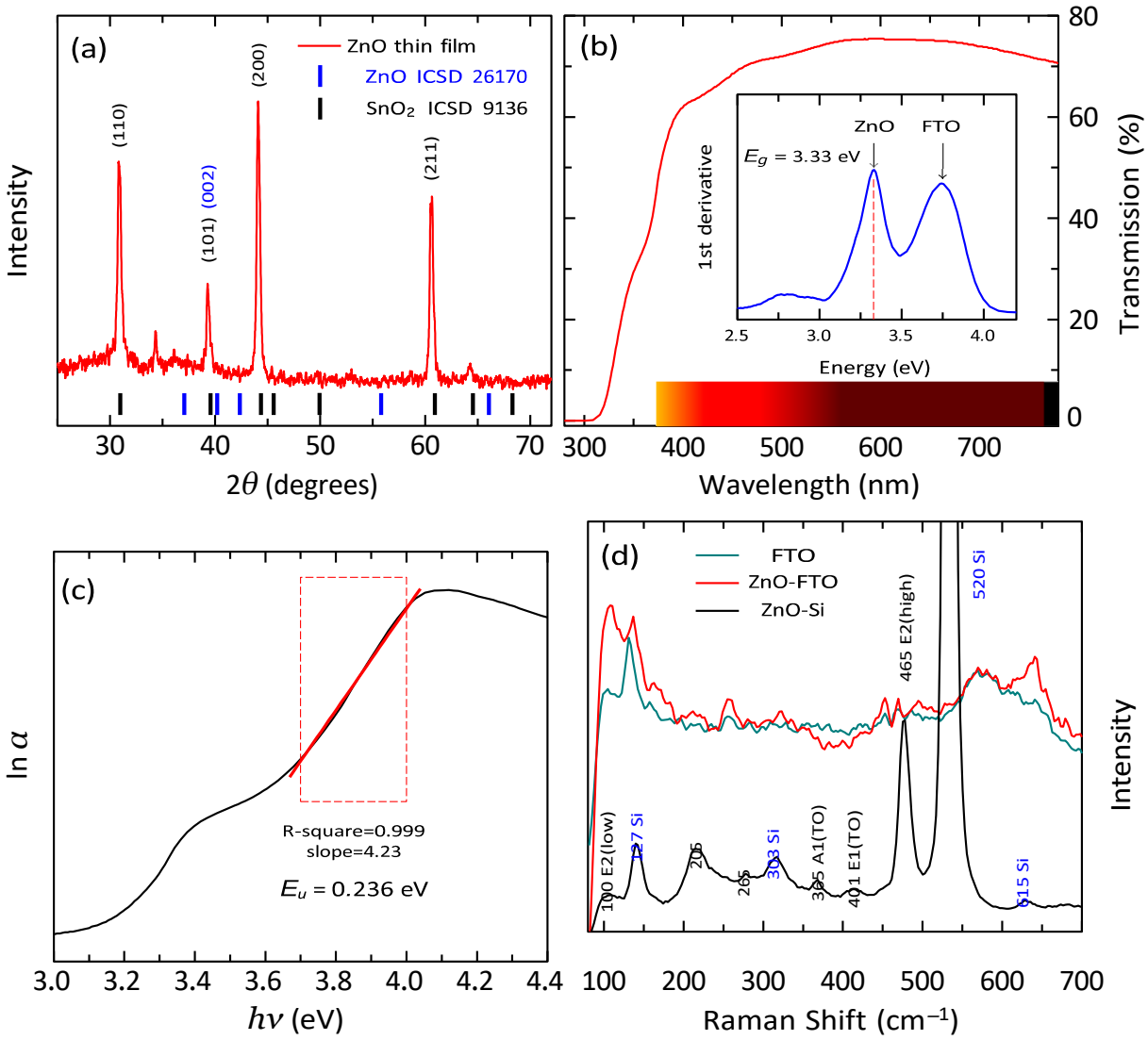

Source: Author.

As will be discussed later, the films consist of agglomerated nanoparticles, resulting in numerous grain boundaries. Due to the crystalline lattice symmetry disruption, these boundary regions contain numerous structural defects acting as electron traps, creating defect states located a few millivolts below the conduction band (58).

These localized states within the bandgap give rise to tail states at the band edges, extending into the optical band. These tails cause an exponential reduction in the absorption

coefficient, resulting in a characteristic energy known as the Urbach energy (E_u). Therefore, E_u is a parameter that correlates band tail phenomena with lattice disorder and crystal defects. It can be calculated using the Urbach empirical equation:

$$\alpha = \alpha_0 e^{h\nu/E_u}, \tag{2.2}$$

where α_0 is a constant. From eq. 2.2, the Urbach energy can be determined as the reciprocal of the slope of the line that fits the relationship ln α vs. $h\nu$ in the linear region of the exponential curve (as shown in Fig. 6c). The calculated mean value of E_u was approximately 0.236 eV. In the literature, E_u values typically fall within the range of 0.1 to 0.4 eV (59, 60). Higher E_u values suggest a higher degree of lattice disorder and a more significant contribution of defects in the localized states within the optical gap.

It is worth noting that the Urbach energy is also influenced by particle size. Smaller nanoparticles experience stress and deformation during formation, leading to increased structural disorder and, consequently, higher E_u values (60, 61). These findings align with existing literature and are consistent with the other results.

Figure 6d displays the Raman spectra of the FTO substrate (red line), the ZnO film on the FTO substrate (blue line), and the ZnO film on the Si substrate (black line). ZnO exhibits a wurtzite structure characterized by C6v4 (P63mc) space group symmetry, with four atoms constituting its primitive cell. Following group theory, at the wavevector $k = 0$ (Γ) in the ZnO phonon dispersion relation, the optical phonons are described by the following irreducible representation: Γ = A1 + E1 + 2E2 + 2B1, where only the B1 modes not Raman active. Furthermore, the A1 and E1 are polar modes and can be further divided into transverse optical, A1(TO) and E1(TO), and longitudinal, A1(LO) and E1(LO), components. Both of these polar modes are not only Raman active but also infrared active. Additionally, E2 is a non-polar mode that exclusively exhibits Raman activity. This branch can be further subdivided into two components: one at lower frequency E2(low), attributed to the heavy Zn sublattice, and another at higher frequency E2(high), associated with the vibration of oxygen atoms (62, 63).

The vibrational peaks at approximately 127, 303, 520, and 615 cm^{-1} are assigned to the Si substrate. Additionally, it is possible to observe the frequencies of the followingfundamental optical modes of ZnO: E2(low) at 100 cm^{-1}, E2(high) at 465 cm^{-1}, A1(TO) at 356 cm^{-1}, A1(LO) at 574 cm^{-1}, E1(TO) at 401 cm^{-1}, and E1(LO) at 583 cm^{-1}. These values are in agreement with the results reported in the literature (63).

Šćepanović *et al.*(64) employed Raman spectroscopy to investigate structural dis- order in ZnO nanoparticles obtained by mechanical milling. Their findings indicated that the broadening and redshift observed in the E2(high) and E1(LO) modes were associated with increased disorder in the ZnO crystal resulting from mechanical milling. They used reference values of 438 and 590 cm^{-1}. Therefore, based on the vibrational mode values obtained in this study, it is reasonable to suggest that the deformation and defects induced by the chemical growth of ZnO nanoparticles also lead to broadening and redshift effects.

2.3.2 Electrical properties

Figure 7a presents an atomic force microscopy (AFM) scan conducted in contact mode, covering a $2\,\mu m \times 2\,\mu m$ area of a ZnO thin film. This image reveals the granular structure of the film with a root mean square (RMS) roughness of 19.4 nm.

In contrast, Fig. 7b displays an EFM image obtained in lift mode through a two-pass scan. In the first pass, the probe operated in tap mode to scan the topographic features. During the second scan, the cantilever was elevated to a height of 40 nm to minimize the influence of van der Waals forces. This elevation allowed for detecting variations in the electrical force gradient, effectively isolating the electrical effects from topography (65). The scan was performed while

applying a voltage of –4 V to the tip. The image in Fig. 7b shows the distribution of electrostatic forces on the film's surface.

The dark contrast observed in the grain face region indicates a weak repulsive electrostatic interaction, while the bright contrast in the grain boundary region indicates a strong repulsive interaction (66). This contrast intensity variation confirms the different accumulation of charge in the grains and GB, which, in turn, leads to distinct charge transport processes across the interface. To investigate this electrostatic interaction, scans were also conducted while applying a positive tip voltage of +4 V. However, only the image generated with negative polarization is presented due to the contrast intensity. As an intrinsically n-type semiconductor, ZnO presents the tendency to trap negative charges on its surface, intensifying the repulsive electrostatic interaction.

The height profile and phase shift data for the lines drawn on the maps are overlaid on the images. The depth and height along the z-axis range from –40 nm to +40 nm. The phase shift peaks observed between grains, indicating an increase in the electrostatic interaction intensity, clearly demonstrate the accumulation of charge in that region.

Figure 7 – (a) Topographic height of a ZnO film (taken in contact mode), clearly depicting the presence of grains and grain boundaries; (b) EFM image of the ZnO film corresponding to V_{tip} = 4 V, showing a variation in the electrostatic interaction at grain boundaries. Overlaid on the images are line profiles corresponding to the height and phase shift.

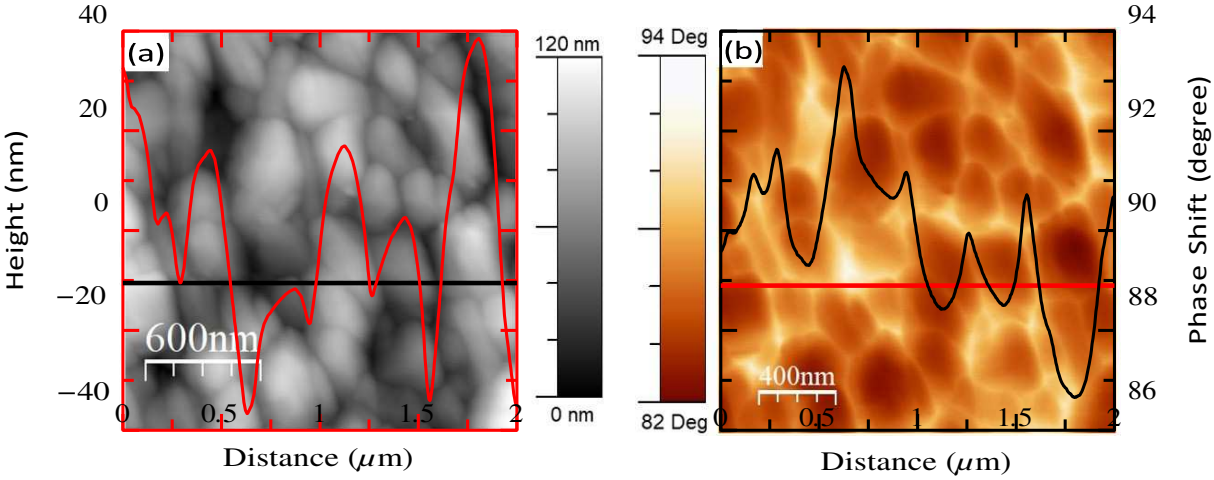

Source: Author.

c-AFM was employed to create a current map (Fig. 8a) applying a +100 mV voltage to the substrate to gain deeper insights into the charge-trapping process. In Fig. 8a, the brightest regions on the current map represent the highest current signals. It is apparent from the map that there is a non-uniform distribution of current flow at a fixed bias voltage. This non-uniformity arises because the lateral changes influence the conductive pathways along the sample surface in the rectifying contacts between the tip and ZnO nanoparticles. These variations result in different current flows through the metal-semiconductor contacts (67). This non-uniform conduction pattern suggests that the grains consist of agglomerations of nanoparticles. This inference is corroborated by the AFM phase imaging (PI-AFM) data, as depicted in Fig. 8c.

PI-AFM is sensitive to the tip and surface interaction, operating in tapping mode to map surface elasticity space variations. This technique detects phase shifts associated with the proximity of the probe to the material and effectively maps local physical layers and surface morphology (68). The phase image of the ZnO film surface, as seen in Fig. 8c (right), reveals numerous phase transitions. A transition from one layer to another within a grain corresponds to an approximately 9.09° phase shift, indicating a change in the interaction between the tip and the surface of a single ZnO nanoparticle. The yellow circles highlight what appears as a continuous grain (Fig. 8c - left) is revealed in the phase image (Fig. 8c - right) to be a cluster. This localized surface phase morphology supports the assumption that each grain consists of an agglomeration of ZnO nanoparticles, contributing to the non-uniform conduction pattern observed in c-AFM.

Figure 8 – (a) c-AFM image of a ZnO film surface; (b) I-V characteristics of grain and GB using the c-AFM tip showing a rectifying behavior. Inset: A semi-log plot of forward bias I-V characteristics obtained from grain and the GB; (c) AFM image highlighting one grain inside the yellow circle (left side) and AFM phase image of the same grain, revealing smaller contours that indicate the presence of agglomerated nanoparticles (right side); (d) AFM image of a zoomed-in grain on a ZnO film (left side) and a localized current distribution map of both the ZnO grain and grain boundary (GB), as determined by c-AFM (right side). Overlaid on the images are line profiles corresponding to topographic height and current.

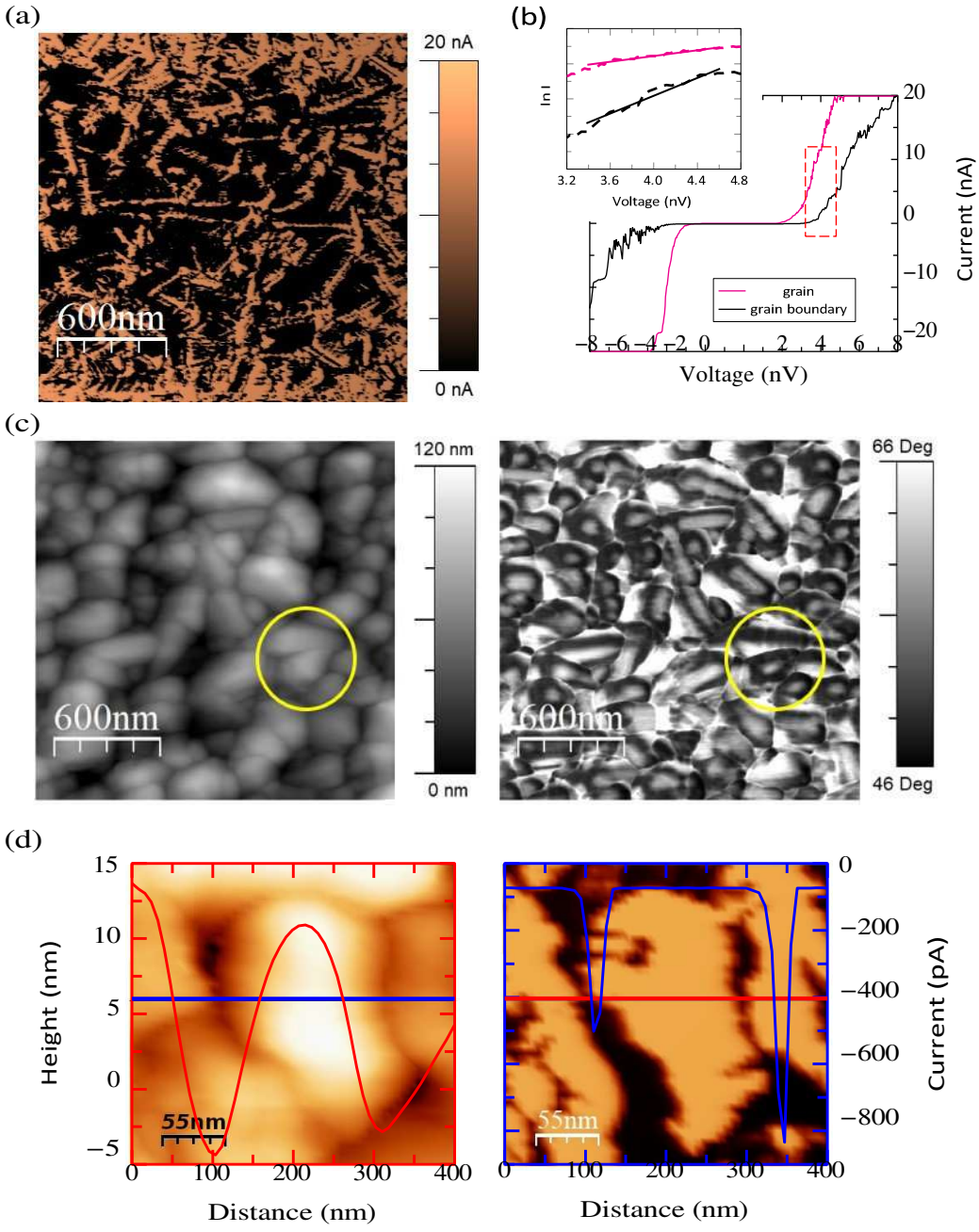

Source: Author.

To investigate conduction in grain faces and GB, the area of a grain was magnified (Fig. 8d - left side), and the current distribution across the grain face and grain boundary was recorded in a local scan. The current map in Fig. 8d (right side) confirms higher conduction in the region of the grain face (clear contrast), as further demonstrated by the topographic profile and the current profile overlaid on the images. It is possible to observe a gradual increase in current away from the grain boundary. The sharp drop in current values at the GB indicates the confinement of charges, making the conduction process through the interface more challenging.

Structural defects, such as vacancies and interstitial atoms, are crucial in all oxide materials, including ZnO. As previously discussed, defects in the crystalline lattice introduce optically active states within the bandgap, effectively creating potential wells for charge carriers. This can impede the efficient collection of charge across the grain boundary (69, 70).

These localized states at grain boundaries give rise to a spatial charge region responsible for forming a potential barrier between the grain face and the grain boundary. At the interface between the grain and grain boundary, the bending of the conduction band due to this potential barrier can influence the charge transport process within the material (18). The local current-voltage (I-V) characteristics in grains and grain boundaries were recorded using c-AFM to quantify the difference in potential barrier height between the grain and grain boundary. The tip was ramped under a ±0.4 V bias voltage, resulting in the I-V curves shown in Fig. 8b.

These curves exhibit clear rectifying behavior due to forming a Schottky-like junction between the Pr-Ir tip and the ZnO film (a metal-semiconductor contact). According to the thermionic emission (TE) theory, the current through the junction barrier as a function of the applied voltage is given by the following equation (17, 18):

$$I = I^S \exp\left(-\frac{qV}{nk_BT}\right) - 1 \ , \tag{2.3}$$

where the saturation current I^S depends on the potential barrier and is related to it according to:

$$I^S \propto \exp\left(-\frac{\Phi}{nk_BT}\right) \ , \tag{2.4}$$

where Φ is the Schottky barrier height (SBH), n is the ideality factor, k_B is the Boltzmann constant and, T is the temperature. According to the TE model, the Schottky diode parameters n and Φ are presumed independent of voltage. These parameters are derived, respectively, from the slope and intercept of the line that best fits the relationship between $\ln I$ and V (as illustrated in the inset of Fig. 8b), expressed as:

$$\ln I = \frac{qV}{nk_BT} + \ln I^S. \tag{2.5}$$

Considering that both the grain and the GB form similar contacts, the change in potential barrier height $\Delta\Phi$ can be calculated as:

$$\Delta\Phi = \mathrm{n}k_B\mathrm{T}\ln\frac{I_G^S}{I_{GB}^S} \tag{2.6}$$

where I_G^S and I_{GB}^S are the saturation currents at the grain and the grain boundary (19).

The ideality factor serves as an indicator of the non-ideal behavior exhibited by the Schottky diode. Adjusted values for *n* in both the grain and the grain boundary were determined to be 2.20 ± 0.1 and 5.0 ± 0.3, respectively. Deviations from ideality can be attributed to the specific current conduction mechanism under consideration. The TE model, which solely considers the thermionic emission mechanism while disregarding tunneling, recombination processes, and the series resistance at the metal-semiconductor junction, results in a higher ideality factor (59). Consequently, since defect states concentrated within grain boundaries act as charge traps, the *n* factor for the GB is slightly higher than that for grain faces. The calculation of $\Delta\Phi$ between the grain and GB was carried out using the mean value of *n* as 3.60 ±0.2.

The application of TE model equations yielded current values of $I_G^S = 1.29 \pm 0.2\ nA$ and $I_{GB}^S = 0.75 \pm 0.2\ nA$. Substituting these values into eq. 2.6, a variation in the potential barrier height of $\Delta\Phi = 50.4 \pm 0.2$ meV was obtained. This variation in $\Delta\Phi$ at the grain/GB interface induces a modulation in the contact potential difference at the film surface, as observed through KPFM measurements.

To further investigate the nanoscale electronic properties of the ZnO film, KPFM measurements were conducted, and the outcomes are shown in Fig. 9. KPFM enables simultane- ous mapping of topography and the measurement of local contact potential differences between the scanning tip and the sample. This technique has been extensively utilized in investigating photovoltaic materials (71, 72). KPFM measurements were conducted in single-pass mode, with an AC voltage of +1 V applied to the Pt-Ir-coated cantilever.

From the measured contact potential difference (V_{CPD}) between the tip and the sample, it was possible to calculate the work function of the ZnO film (Φ_{ZnO}) using the equation $\Phi_{ZnO} = \Phi_{tip} - eV_{CPD}$, where Φ_{tip} is the work function of the Pt-Ir tip, and *e* represents the electronic charge.

The height and potential images are presented in Figs. 9a and 9b, respectively. The height and potential profiles obtained from the lines in Figs. 9a and 9b are overlaid on the images. The profiles reveal a modulation in contact potential within the grain and GB regions. The V_{CPD} potential values for the grain face and GB were found to be 164 mV and 213 mV, respectively. Given that the work

function of the calibrated Pt-Ir tip is $\Phi_{tip} = 4.1$ eV, the work function of the ZnO film on the grain face (Φ_G) and at the GB (Φ_{GB}) was determined to 3.93 eV and 3.89 eV, respectively.

Figure 9 – (a) KPFM topographical image of 4 layers thick ZnO film; (b) corresponding contact potential difference map. Overlaid on the images are height and contact potential variation line profiles.

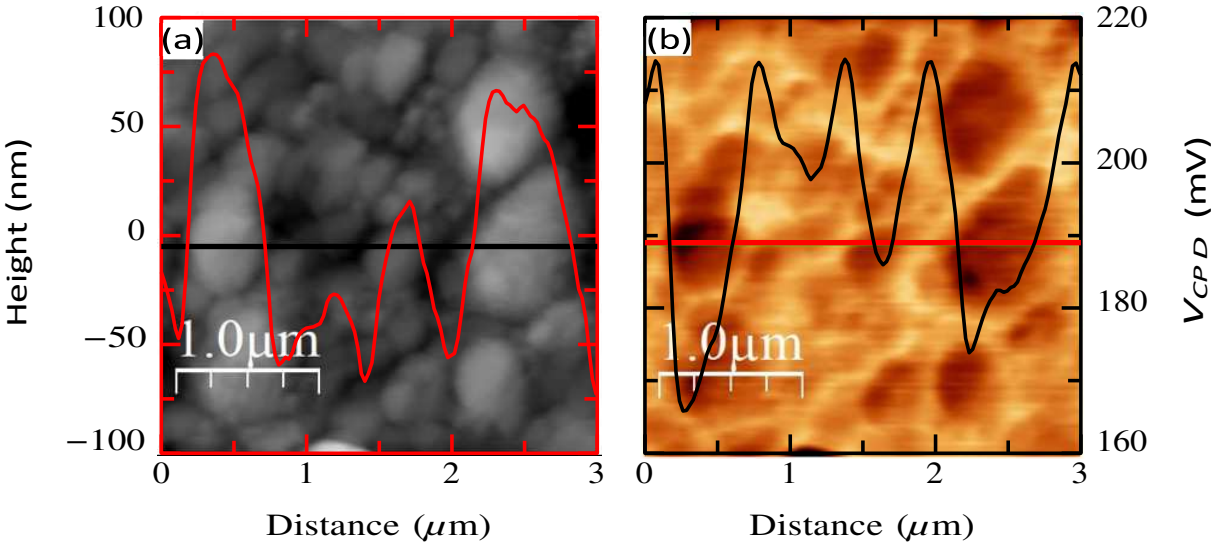

Source: Author.

Notably, Fig. 9b showcases a distinct variation in surface potential at the nanoscale. The region with more pronounced contrasts on the nanostructured surface (the GB region) exhibits a lower work function than the surrounding areas. The average value estimated for the film's work function is consistent with values reported in the literature for ZnO (5, 6).

In the extensive electrical characterization of ZnO film-based nanostructures, most studies focus on macroscopic parameters rather than local ones like grains and grain boundaries. This emphasis on macro parameters complicates data comparison and correlation. Additionally, the electrical properties are not solely influenced by grain boundaries; they are also affected by morphological and structural characteristics, film thickness, annealing temperature, and the introduction of dopants. Table 1 outlines electrical parameters derived from the observed rectifying behavior in I-V curves and extracted from the TE model for diverse ZnO-based nanostructures in the literature.

In studies that identified the formation of grains and grain boundaries within ZnO- based thin films (first three lines of Table 1), localized I-V measurements verified the establishment of Schottky contacts with small variations in the height of the local potential barrier between grain and GB. The values are very close across the cited references despite other properties presented. The standout feature is the saturation current values obtained in this work. Both in grains and grain boundaries, the local current gain reaches approximately 10^3, affirming the feasibility of producing high-quality films with good charge transport characteristics and effective rectifying behavior for optoelectronic applications. This achievement is accomplished through a straightforward and cost-effective technique of spin coating.

Within this same group, it is possible to discern the impact of defect states introduced by grain boundaries on the work function values of the films. As explained earlier, these defect states alter the semiconductor's Fermi level, shifting it toward the conduction band. Consequently, the local work function values at grain boundaries are slightly lower, by a few millivolts, compared to the local values at grains. This local fluctuation in the work function at grain boundaries signifies electronic heterogeneity across the film surface, reinforcing the consistency with the other findings presented.

Table 1 – Electrical parameters acquired from I-V curves at grain and grain-boundary regions. Comparison between results obtained in this work (*) and studies published in the literature. ZTO = ZnO:SnO_2; AZO = Al-doped ZnO; SZT = Ti-doped ZnO-SnO_2.

ZnO-based structure	Deposition technique	E_g (eV)	I_G^S (nA)	I_{GB}^S (nA)	$\Delta\Phi$ (meV)	Φ_G (eV)	Φ_{GB} (eV)	Ref.
ZnO	Spin coating	3.33	1.29	0.75	50.40	3.93	3.89	*
ZTO	Magnetron sputtering	3.15	0.054	0.032	36	4.98	-	(19)
AZO	Magnetron sputtering	-	0.079	0.041	50	-	-	(17)
SZT	Spin coating	4.1	-	-	0.56	-	-	(73)
ZnO	Atomic layer deposition	-	-	-	44	-	-	(74)
AZO	Magnetron sputtering	-	-	-	0.98	-	-	(75)

Source: Author.

2.3.3 Energy band diagram and local band bending

According to the Schottky-Mott theory (14, 15), when dealing with an n-type semiconductor where $\Phi_M > \Phi_S$ (where Φ_M and Φ_S are the metal and semiconductor work functions), the metal-semiconductor contact exhibits rectifying behavior, indicating the formation of a potential barrier. Indeed, due to the work function values observed for the ZnO films and as demonstrated by the I-V curve in Fig. 8b, a rectifying contact was established between the Pt-Ir tip and the ZnO surface.

]Figure 10 provides a possible energy band diagram that illustrates the process of barrier formation once equilibrium is achieved at the local metal-grain interface and metal-grain boundary interface. Upon bringing the metal tip into contact with ZnO, electrons with higher energy from the semiconductor's conduction band flow into the metal until the Fermi levels align. As electrons transfer from the semiconductor to the metal, the concentration of free electrons near the interface diminishes, leading to a displacement of the Fermi level (E_F) away from the conduction band edge (E_C).

In thermal equilibrium, E_F remains constant, causing E_C to shift upward. Since the semiconductor's optical gap and electron affinity remain unchanged after contact with the metal, the valence band edge (E_V) also shifts upward in parallel with E_C along with the vacuum level. In a metal-semiconductor system in thermal equilibrium, the vacuum level must maintain continuity across the transition region. Consequently, to ensure continuity, the semiconductor-side vacuum level must gradually approach the vacuum level on the metal side, resulting in band bending. The difference in vacuum levels, equivalent to the difference in work functions, dictates the local band bending (10, 16).

Figure 10 – Energy band diagram scheme of the local contact between the metal tip and the n-type ZnO film in grain and grain boundary region (red line).

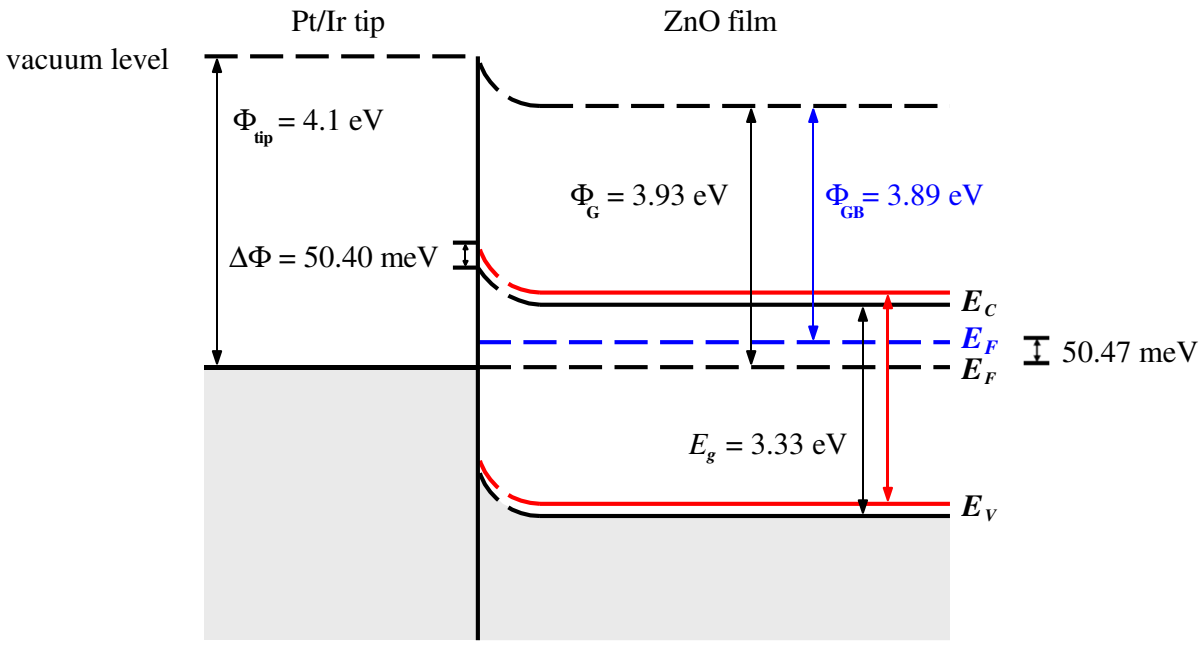

Source: Author.

The accumulation of defect states within the grain boundary increases the carrier density. It shifts the Fermi level of the semiconductor closer to the conduction band (by approximately 0.236 eV, as indicated by the calculated Urbach energy). This shift reduces the local work function value in that region. In this area, achieving E_F alignment necessitates a more substantial band bending, potentially influencing local electrical transport. Based on the provided work function values (Φ_{tip}, Φ_G, and Φ_{GB}), a local band bending of 0.169 eV in the grain and 0.219 eV at the GB were found. The band bending at the GB region is approximately 50.47 eV greater than the value at the grain face, consistent with the difference in potential barrier height computed using the thermionic emission theory (50.40 meV).

While there is limited literature on characterizing local electrical and charge transport parameters in zinc oxide films via local probe microscopy studies, it is possible to analyze and compare data related to potential barrier height, local current saturation values, and work function values in structures involving ZnO and other oxide materials (19, 17, 42, 76).

2.4 Conclusions

This work demonstrated the presence of GB in ZnO films grown on a conductive substrate and how they impact the current and potential barrier at the nanoscale. Topographic images and EFM measurements confirmed the presence of GB and charge trapping in the region. The presence of defect states that result in charge confinement and control transport through the film was numerically

indicated by the Urbach energy (0.236 eV). In an FTO/ZnO/Pt-Ir structure, the formation of a Schottky-type junction between the semiconductor ZnO and Pt-coated tip was evident. Measurements of the variation of the KPFM surface potential confirmed the formation of the Schottky junction based on the work function values obtained (ΦG = 3.93 eV and ΦGB = 3.89 eV). Band bending in the GB was confirmed by local I-V curves obtained from c-AFM measurements at a fixed point but at many randomly chosen locations. The local current values in the grains (I_G^S=1.29 ± 0.2 nA and GB (I_{GB}^S=0.75 ± 0.2 nA) and the variation in the potential barrier between grain and GB (ΔΦ = 50.40 ± 0.20 meV) indicate that band bending and the variation in surface potential at grain boundaries directly affect charge transport in the films. Data on potential barriers in structures such as grain boundaries, commonly found in oxide-based films, represent significant advances in understanding nanoscale charge transport in this class of semiconductors. Therefore, the present study is expected to contribute to fabricating high-mobility transparent electrodes based on ZnO thin films, TCOs, transparent photodetectors, oxide-based solar cells, and other optoelectronic devices.

3 OHMIC-TO-SCHOTTKY MODIFICATION OF ZnO-METAL CONTACT MODULATED BY FILM THICKNESS

The present work systematically investigated the structure and charge transport behavior at the interface between a Pt-Ir metal contact and transparent zinc oxide (ZnO) electrodes deposited on a conductive fluorine-doped tin oxide (FTO) substrate with one, four, and eight ZnO layers. Electrostatic force microscopy (EFM), Kelvin probe force microscopy (KPFM), and conducting atomic force microscopy (c-AFM) techniques were employed to explore the nanoscale surface electrical properties. The variation in thickness led to changes in the type of contact formed between metal and semiconductor (M-S), which went from ohmic to rectifier with the increase in the number of layers. The modulation in the type of M-S contact formed was mainly due to the presence of grain boundaries (GB) during film formation. EFM measurements revealed the presence of charge trapping within the grain boundary region, suggesting localized band-bending effects. KPFM measurements obtained local work function values, which were slightly higher in the GB region in all samples, attributed to the shift of the Fermi level towards the conduction band caused by the defect states inserted by the GBs. The influence of the thickness synthesis parameter on the optoelectronic and charge transport properties of conductive and transparent ZnO electrodes is demonstrated, and its importance in the formation of M-S contacts that make zinc oxide a versatile semiconductor, which finds different applications, depending on the type of metal-semiconductor contact formed.

3.1 Introduction

Zinc oxide is an intrinsically n-type semiconductor, exhibiting a large direct band gap of 3.37 eV, a high exciton binding energy of 60 meV, and robust charge mobility, enabling the formation of thin films with optical transparency (77, 78, 30). Due to its outstanding optoelectronic and electrical properties, it finds applications in blue/UV light-emitting diodes and lasers (79, 80), transparent conducting oxide (TCO) (17, 49), and selective charge layers on solar cells (81, 82). All these technologies require metal contacts, and to achieve high-performance devices, understanding how electrical contacts are influenced by the nature of ZnO surfaces and ZnO-metal interfaces is crucial.

ZnO thin films can form either ohmic or Schottky contacts with metals. However, for efficient current injection, nanoscale devices must operate with low contact resistance and precise control of band bending. Many ZnO-based devices require electrodes with good ohmic contacts, as low contact resistance, insignificant compared to the bulk resistance of the semiconductor, can result in a lower voltage drop across the electrode, thereby increasing the current injection efficiency of the device (9, 10). The utilization of ohmic contacts in photoconductive-type photodetectors by Reyes et al.

(11) revealed current gain, albeit at slower response speeds. Conversely, photodetectors with Schottky contact electrodes generally exhibited faster response speeds and less noise current, as reported by Su et al. (12). Hwang and Hong (13) noted that a significant Schottky-barrier height (SBH) at the metal-semiconductor interface of Schottky- barrier photodetectors leads to a small leakage current and high breakdown voltage, thereby improving device performance.

The fabrication of stable rectifier metal contacts poses a considerable challenge, as reported in the literature (13, 83). Schottky-type contacts are influenced by the Fermi-level pinning effect introduced by the presence of defect states. Defect states introduced by dopants and grain boundary regions arising from the thermodynamic driving force of film growth are inserted into the optical gap of semiconductors (37, 84, 19). These charge-trapping regions result in band bending that can control the local charge transport process through the ZnO-metal electrode junction (85).

Various parameters influence the optical and electrical characteristics of ZnO films, including annealing temperature, deposition technique, and film thickness (8). The surface properties of ZnO play a crucial role in modulating the contact characteristics between ZnO and metals. Therefore, controlling the film deposition conditions in the fabrication of ohmic and Schottky ZnO-metal contacts can contribute to developing high-performance devices (86).

Several research groups have investigated metal contacts manufactured from ZnO- based nanostructures in recent studies. Li et al. (86) analyzed the influence of metal coating on ZnO films grown on silicon substrates through hydrothermal reactions, revealing the impact of the type of metal on the formation of ohmic or Schottky contacts. The researchers also associated the contact formed at the ZnO/metal interface with the emission properties of ZnO nanostructures, finding that the UV ZnO near band edge (NBE) emission is affected by whether the contact is ohmic or Schottky. Su et al. (9) demonstrated the modulation of ZnO/Au contacts from ohmic to Schottky through plasma surface treatments on ZnO thin films prepared by radiofrequency plasma-assisted molecular beam epitaxy (RF MBE). They observed the ohmic behavior of ZnO/Au contacts exposed to Ar/N2 plasma and a transition to rectification behavior when treating the ZnO surface with O_2 plasma. Lin et al. (87) induced the ohmic-rectification conversion of MoS_2/ZnO contacts by treating ZnO-nanorod samples in a H_2O_2 solution, enhancing the rectification performance of MoS_2/ZnO nanorod devices and increasing their responsivity to solar irradiation.

This work used scanning probe microscopy in EFM, KPFM, and c-AFM modes to analyze the ohmic to Schottky conversion of ZnO/PtIr (platinum-iridium) contacts. This modu- lation was achieved by controlling the thickness of ZnO films spin-coated on FTO conductive substrates. The influence of the number of layers on the charge transport properties of contacts was also investigated. EFM measurements scanned surface topography, revealing evidence of charge trapping on grain boundary (GB) regions and confirming the presence of defect states that shift the Fermi level of the semiconductor toward the conduction band. This shift influences the work function and,

consequently, the metal-semiconductor (M-S) contact. KPFM measurements were performed to confirm the formation of an ohmic or rectifying metal-semiconductor contact and to highlight the band bending occurring due to the potential barrier formed on M-S rectifying contacts, influencing the charge transport process. Ohmic and rectifying behaviors were recorded in IV curves obtained by c-AFM. Thermionic emission (TE) model equations provided informa- tion about the charge transport of Schottky barrier devices, extracting local saturation current and local potential barrier height data. Additionally, ultraviolet-visible (UV-vis) spectroscopy was employed to determine the optical properties of films, while X-ray diffraction (XRD) and Raman spectroscopy were performed to determine their structural properties.

This work aims to enhance understanding of electrical parameters and the local charge transport process in ZnO films widely used as electrodes in optoelectronic and other devices. These films can be produced using a simple technique while exhibiting good conduction characteristics. Notably, the film thickness was identified as a parameter that can control the metal-semiconductor contact and influence the charge transport properties.

3.2 Experimental procedure

3.2.1 Synthesis of zinc oxide nanoparticles solutions and films

The zinc oxide nanoparticles were prepared using the coprecipitation method, fol- lowing a procedure similar to the one reported in the literature (32, 43). Zinc acetate dihydrate ($Zn(CH_3COO)_2 \cdot 2H_2O$, $\geq 99\%$, Neon) and potassium hydroxide (KOH, Sigma Aldrich) in absolute methanol (CH_3OH, Sigma-Aldrich) were employed. The synthesis initiated with the preparation of a $Zn(CH_3COO)_2 \cdot 2H_2O$ solution (2.97 g) in methanol (125 ml) heated to 60°C. Simultaneously, a KOH solution (1.51 g) in methanol (65 ml) was heated to 60°C. The KOH solution was then added to the zinc acetate solution for 30 seconds. Following the addition, the mixture was gently refluxed at the same temperature and stirred for 3 hours, leading to precipitation. The stirring bar was removed, and the mixture stood at room temperature for 24 hours. After careful decanting, the precipitate was re-suspended in methanol (125 ml) and allowed to settle for an additional 24 hours, after which the methanol was removed, ensuring that the precipitate was drained without completely drying it.

The resulting precipitated ZnO nanoparticles were redispersed in 1,2-dichlorobenzene (anhydrous 99%, Sigma Aldrich) at a concentration of 50 mg/ml. To maintain nanoparticle stability, 2-(2-methoxyethoxy)acetic acid (MEAA, Sigma Aldrich) was added at a concentration of 4% w/w relative to ZnO. The addition of MEAA provided solutions stability for months under atmospheric conditions, facilitating film preparation through coating methods such as spin-coating.

Fluorine-doped tin oxide (FTO) coated glass substrates (surface resistivity approximately 7 Ω/sq, dimensions 20 mm×10 mm×2.5 mm, Sigma Aldrich) served as transparent conductive substrates. Before film deposition, all substrates underwent ultrasonic cleaning with deionized water and isopropyl alcohol. The deposition process involved spin-coating 30 μl of the zinc oxide solution onto FTO substrates using an Ossila spin coater without vacuum at 1200 rpm for 30 seconds. Subsequently, the deposited films underwent heat treatment on a hot plate at 310 ˚C for 30 minutes to polymerize the zinc oxide film (32), resulting in the sample referred to as ZnO1 (one layer of ZnO film).

This deposition process was repeated four times, interspersed with heat treatment steps at 310 ˚C for 5 minutes, yielding samples labeled ZnO4 (four layers of ZnO film). After the final layer, the films were treated at the same temperature for 30 minutes. The same process was iterated eight times to obtain ZnO8 samples (eight layers of ZnO film), with 30 minutes of heat treatment after the last layer.

3.2.2 Characterization techniques

Transmittance spectra were obtained at room temperature using a UV-Vis spectrophotometer Shimadzu model UV-2600, equipped with an integrating sphere (ISR-2600Plus), covering the wavelength range of 220 to 800 nm. Raman spectroscopy was performed using an Alpha 300 Witec system. The excitation source was the 532 nm laser line, delivering a laser power of 0.6 mW with an accumulation time of 2 seconds. X-ray diffraction patterns were recorded using a Rigaku SmartLab SE X-ray diffractometer with a theta-theta goniometer configured in Bragg-Brentano geometry and operated at a power of 1.4 W (40 kV and 35 mA). Co-Kα ($\lambda = 0.1789$ nm) was used as the radiation source.

All nanoscale electrical measurements were carried out using an atomic force microscope Asylum MFP-3D-Bio AFM from Oxford Instruments. Conductive tips (Pointprobe Silicon SPM-Sensor probes, NanoWorld) were used, featuring a tip radius of 20 nm, stiffness of 2.8 Nm^{-1}, resonant frequency of 75 kHz, and platinum-iridium (Pt-Ir) coating.

c-AFM measurements were performed in contact mode. The elevation mode was used for KPFM and EFM measurements, with a height of 40 nm above the film surface. Local I-V measurements were conducted with the Pt-Ir conductive tip and the FTO substrate configured as the top and bottom electrodes, respectively. This configuration formed the Pt-Ir/ZnO/FTO heterojunction through which electron transport was analyzed. These measurements were conducted at numerous selected locations on each sample (ZnO1, ZnO4, and ZnO8), with scan speeds varying from 0.2 to 0.5 Hz.

3.3 Results and discussion

3.3.1 Structural and optical properties

Figure 11a shows the X-ray diffraction pattern obtained for thin films ZnO1, ZnO4, and ZnO8 deposited on an FTO conductive substrate. The diffraction peaks associated with the {110}, {101}, {200}, and {211} crystallographic planes are attributed to the polycrystalline SnO_2:F phase of FTO. These observations align with the tetragonal rutile crystal structure (space group P42/mnm), as confirmed by the ICSD card file number 9163.

In addition to the SnO_2 structure, the X-ray diffraction pattern reveals a characteristic wurtzite-type hexagonal crystalline arrangement (space group P63mc) attributed to the ZnO crystal, consistent with ICSD data sheet number 26170. Notably, there is an increase in peak intensity at $2\theta = 40.2^{\circ}$ with an increase in the number of deposition layers. This peak corresponds to the well-known basal planes {002} of ZnO. Notably, the {101} planes of SnO_2:F overlap with the {002} basal planes of the wurtzite structure. This overlap renders the ZnO film less discernible in the ZnO1 film, consistent with a previous investigation (88). However, as the number of layers increases in ZnO4 and ZnO8, the ZnO deposition over the FTO substrate becomes more evident. A slight difference between the ICSD standard file card and the experimental results was noted, presumably due to variations in the unit cell lattice size of the material (45).

Figure 11 –(a) X-ray diffraction patterns of ZnO films on FTO substrate; (b) UV-vis transmittance spectra (inset: 1st derivative showing the absorption of FTO and ZnO).

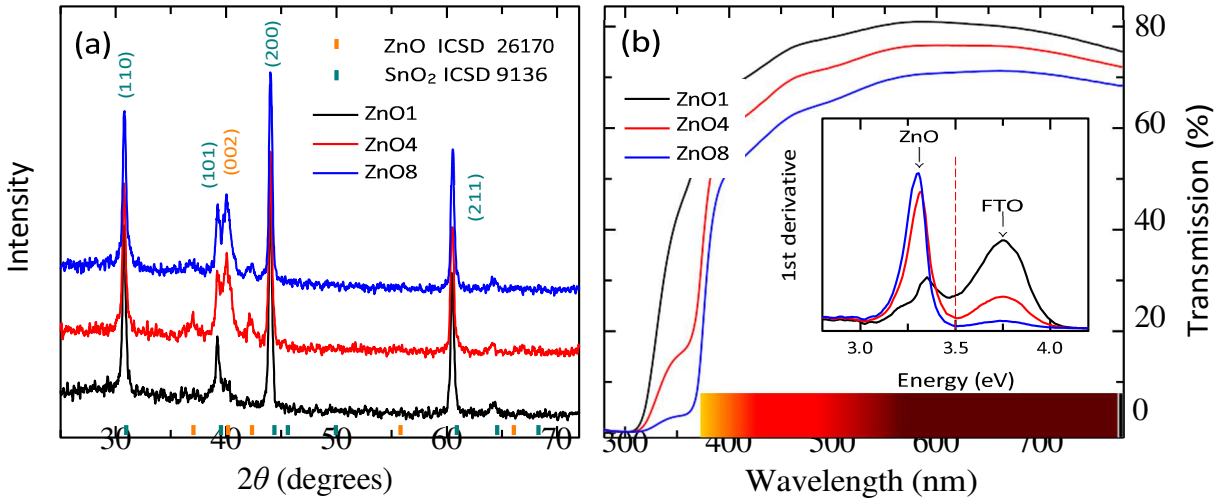

Source: Author.

Figure 11b presents the transmittance spectra in the ultraviolet-visible region of ZnO1, ZnO4, and ZnO8 films, indicating a reduction in transmittance at the characteristic fundamental absorption edge of ZnO (47). Due to the thickness effect, the edge is red-shifted from approximately 371 nm to 376 nm. According to the Beer-Lambert law (48), an increase in thickness results in an extended optical path length, leading to increased light absorption and, consequently, a decrease in the detected transmission signal. In the case of the ZnO films, the transmittance decreased from 80% to approximately 70% with the increase in the number of layers from one to eight.

Furthermore, the shift in the absorption edge may be attributed to grain size and/or carrier concentration effects (89). As AFM and EFM measurements will reveal, all the films consist of nanoparticles with an average size of 50 nm (estimated from a TEM measurement not shown) agglomerated into grains that appear during film formation due to the thermodynamic forces involved in the growth process. Grain boundaries contain numerous structural defects that increase photon scattering, contributing to the decrease in the average transmittance of the films in the visible region. The accumulation of layers increases the number of nanoparticles agglomerated into grains, making the grains larger.

The energy band gaps were calculated by identifying the peaks in the first derivative of the UV-Vis spectrum, as illustrated in the inset of Fig. 11b (88, 50, 51). Peaks at 3.75 eV are attributed to the FTO substrate, which has band gap values falling within 3.6 to 4.0 eV, depending on the level of fluorine incorporation (52). The other peaks are assigned to the absorption by the ZnO films, clearly demonstrating the dependency of the energy band gap on the film thickness. The band gap values decrease with increased layers, measuring 3.34 eV, 3.32 eV, and 3.30 eV for ZnO1, ZnO4, and ZnO8 films.

3.3.2 Electrical properties

The images presented in Fig. 12 (left images) were obtained during the initial pass of an atomic force microscopy measurement in lift mode through a two-pass scan, with the probe in tap mode. These images revealed the granular morphology of the films, with a root-mean-square (RMS) roughness of 19.41 nm for ZnO1, 35.91 nm for ZnO4, and 40.25 nm for ZnO8. Surface roughness increased with film thickness, along with an increase in grain sizes and numbers.

Figure 12 (right images) displays EFM images obtained in the second pass, applying a –4 V voltage between the tip and the film surface while the cantilever oscillates 40 nm above the film without contact. The grain faces appeared in a dark contrast for all samples, indicating a weak repulsive electrostatic interaction. The bright contrast in the grain boundary region indicated a strong repulsive interaction (66), revealing charge accumulation regions along the films

that lead to distinct charge transport properties and metal-semiconductor-type contacts.

The height profile and phase shift data are overlaid on the images - the depth and height along the z-axis range from −40 to +40 nm. The phase shift peaks observed between grains indicate increased electrostatic interaction intensity, suggesting charge accumulation. As the number of layers increased, the phase shift data presented increasing values of 2.60°, 9.09°, and 12.3° for ZnO1, ZnO4, and ZnO8, respectively, corroborating the results.

Due to the crystalline lattice symmetry disruption, grain boundary regions contain numerous structural defects, such as vacancies and interstitial atoms. Defects in the crystalline lattice introduce defect states within the bandgap, effectively creating potential wells for charge carriers (69, 70). As an intrinsically n-type semiconductor, the Fermi level of ZnO is close to the conduction band. Introducing states in the bandgap brings the Fermi level closer to the conduction band, changing the value of the material's work function and, consequently, the M-S type of contact, as evidenced in the KPFM measurements.

Figure 12 – Topographic height images (left) and EFM images (right) showing a variation in the electrostatic interaction at grain boundaries of (a) ZnO1, (b) ZnO4, and (c) ZnO8 films. Overlaid on the images are line profiles corresponding to the height and phase shift.

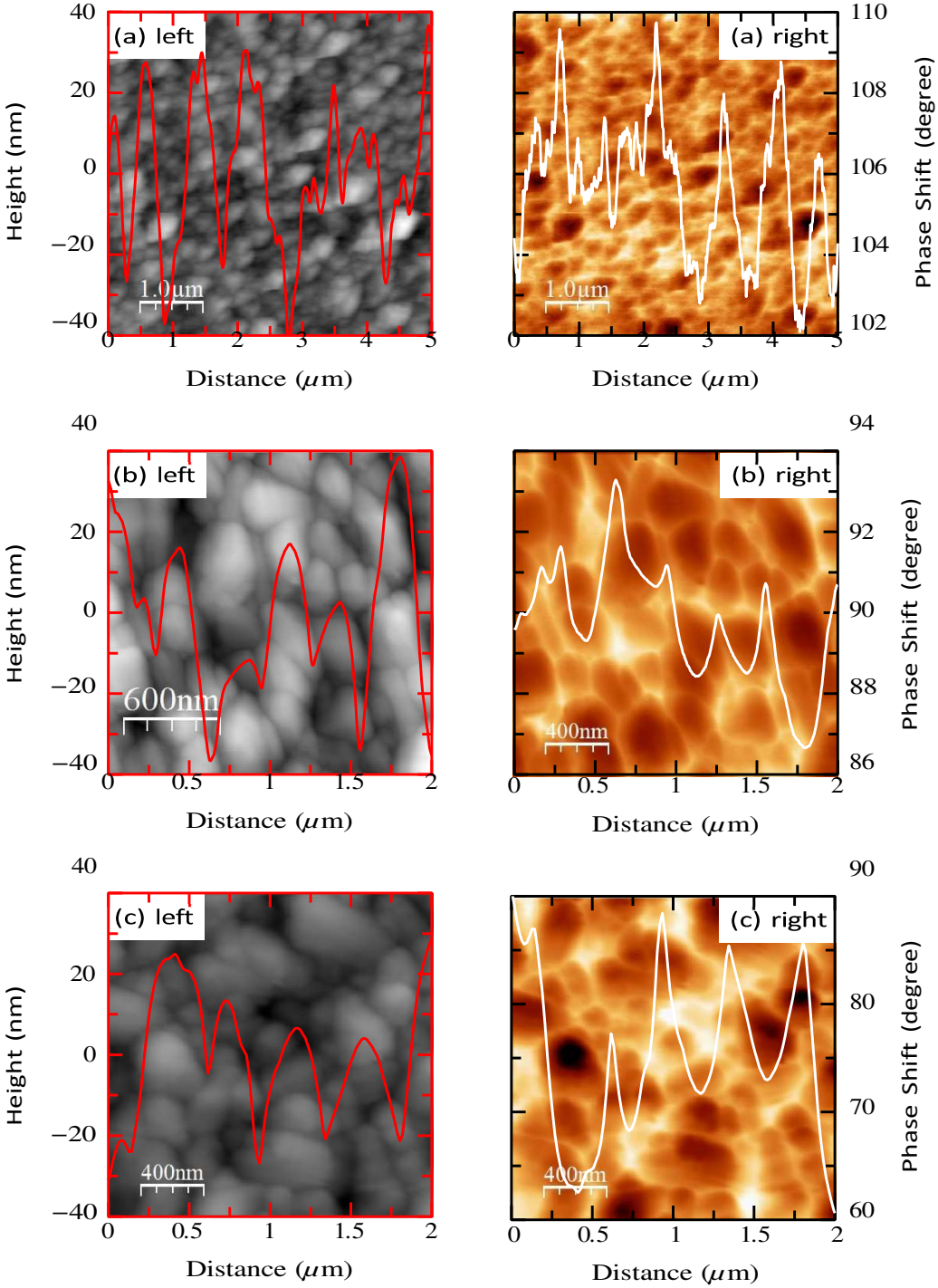

Source: Author.

Kelvin Probe lift mode using an applied AC voltage of +1 V on the Pt-Ir-coated cantilever. The objective was to map the topography (Fig. 13, left side images) while simultaneously recording local contact potential differences (V_{CPD}) between the scanning tip and the sample. KPFM images, featuring overlaid height and potential profiles, are shown in Fig. 13, right side images. An evident modulation in V_{CPD} is observed across the films, attributed to the presence of grain boundaries. Notably, the maps exhibit distinct variations in surface potential at the nanoscale. Grain boundary regions appear as pronounced contrasts on the nanostructured surface.

By applying an external bias, KPFM minimizes the electrostatic interaction between the tip and the surface at each scanning point. This process can be directly interpreted in terms of a localized work function, expressed as:

$$\Phi_{ZnO} = \Phi_{tip} - eV_{CPD}, \tag{3.1}$$

where Φ_{tip} is the work function of the Pt-Ir tip and e represents the electronic charge (90). By substituting V_{CPD} values into equation 3.1, along with the calibrated work function of the Pt-Ir tip, $\Phi_{tip} = 4.1$ eV, the localized work function at grain and grain boundary regions of ZnO1, ZnO4, and ZnO8 films was calculated and is presented in Table 2.

The GB region exhibited lower work function values in each sample than the grain face region. Defect states in these regions introduced defect states in the band gap, shifting the Fermi level toward the conduction band and reducing the work function, defined with reference to the vacuum level. The average work function between grain and GB of the films is presented in Table 2 to evidence the difference between samples of various thicknesses.

The increase in grain size accompanying the growth in the number of layers results in lower work functions in the ZnO4 and ZnO8 films, as discussed earlier, displaying very similar values. Additionally, the work function of the ZnO4 film is slightly lower than that of the ZnO8 film. This difference can be attributed to the agglomeration of nanoparticles in a more concentrated manner, forming larger grains.

Table 2 – Electrical parameters acquired from KPFM and I-V curves of local c-AFM measurements.

Film	Region	Φ^{local} (eV)	Φ^{avg} (eV)	ϕ (meV)	I^S (nA)	$\Delta\Phi$ (meV)
ZnO1	G	4.432	4.421	20.6	-	-
	GB	4.411				
ZnO4	G	3.931	3.906	50.47	1.29	50.41
	GB	3.881			0.75	
ZnO8	G	3.944	3.915	58.71	1.09×10^{-3}	52.34
	GB	3.886			0.40×10^{-3}	

Source: Author.

Figure 13 – KPFM topographical images (left) and corresponding contact potential difference maps (right) of (a) ZnO1, (b) ZnO4, and (c) ZnO8 films. Overlaid on the images are line profiles corresponding to the height and contact potential variation.

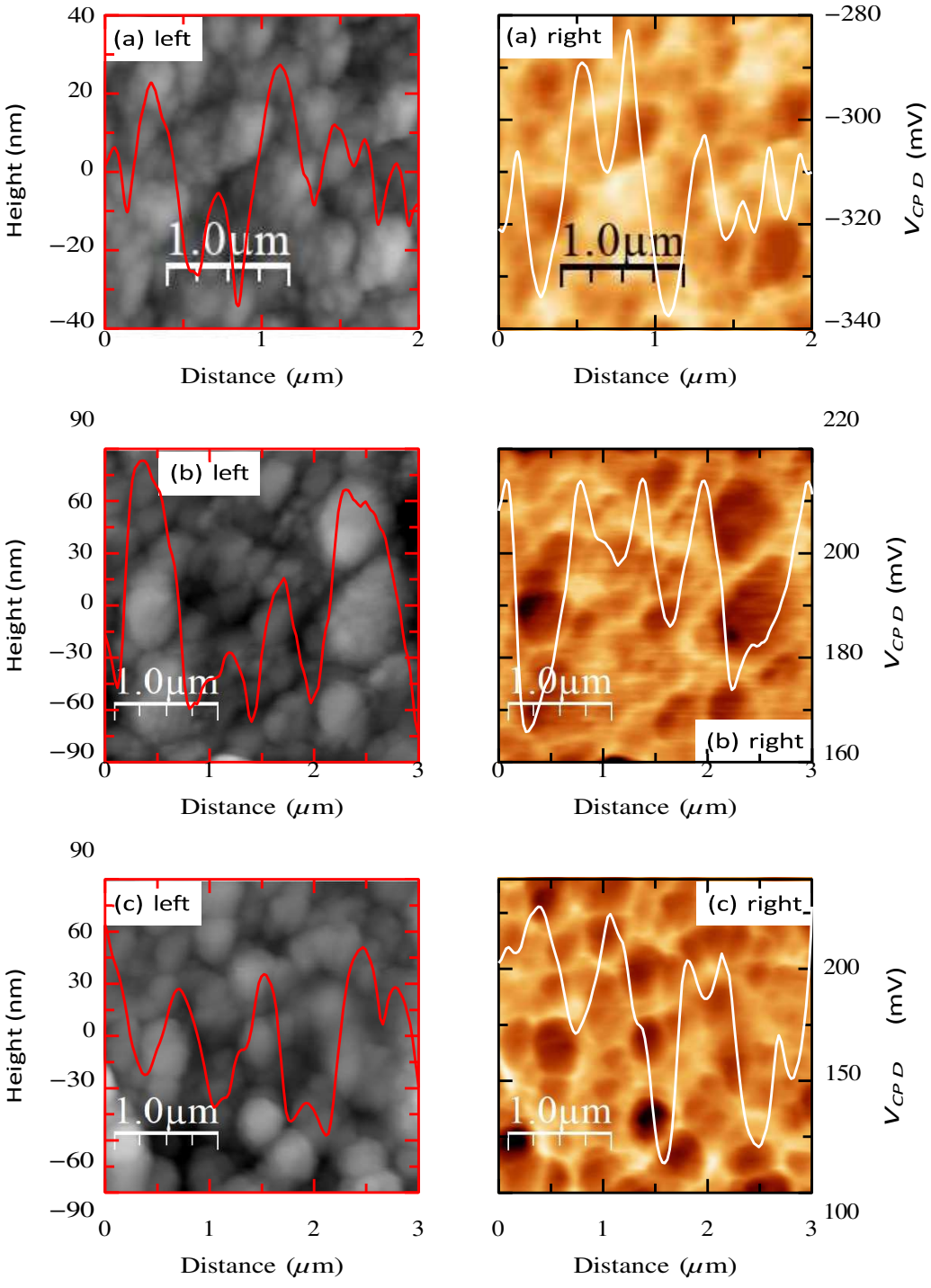

Source: Author.

According to the Schottky and Mott model (10), which describes the potential barrier formed in the contact between a metal and a semiconductor, when an n-type semiconductor has a work function lower than the work function of the metal ($\Phi m > \Phi s$), a rectifying contact is formed between them. In contrast, when ($\Phi m < \Phi s$), a non-rectifying contact, or ohmic contact, is formed. Considering the work function value of the metal and the average work function

value of each film, it can be concluded that there will be the formation of ohmic contact between the Pt-Ir metal tip and the ZnO1 film and the formation of rectifier contacts between the Pt-Ir metal tip and the ZnO4 and ZnO8 films. The I-V curves obtained from c-AFM scans confirm the suggested contact types for each sample.

The charge trapping identified by EFM and KPFM measurements suggests a non-uniform current flow distribution at a fixed bias voltage. The conductive pathways in c-AFM images along the film surface are influenced by lateral changes in the contact between the tip and ZnO nanoparticles, resulting in different current flows through the metal-semiconductor contacts (67). In our previous work (88), c-AFM was employed to create a current map by applying a +100 mV voltage to the FTO substrate, allowing the observation of the non-uniform conduction pattern along ZnO4 samples obtained under the same conditions.

In this study, c-AFM scans were conducted to gain deeper insights into how charge trapping influences the conduction process and the type of M-S contact formed. The local current-voltage (I-V) characteristics in grains and grain boundaries were recorded by applying a +100 mV voltage to the substrates, as depicted in the scheme in Fig. 14a, to study the conduction process through the M-S interface.

From the curve presented in Fig. 14b, it is possible to observe the non-rectifier contact formed between ZnO1 and the Pt-Ir metal tip, with an unmistakable and characteristic linear I-V behavior of an M-S ohmic contact, corroborating with Schottky and Mott theory for $\Phi m < \Phi s$. Here, the current is determined by the resistance of the bulk semiconductor region and is independent of the direction of the applied bias. The value of the bulk resistance is given by the slope of the straight portion in the I-V curve (highlighted region within Fig. 14b). In general, the average work function of ZnO1 film has a value very close to the work function of the metal, offering a minimum resistance to the charge transport, hence the low average slope value. A slight reduction in the local saturation current in the GB region is also noted, possibly due to the defect states that act as charge traps. Low-resistance metal contact with semiconductors results when the barrier height is zero or is small compared to the thermal energy kT. It often occurs when the thickness of the depletion layer contact barrier is reduced sufficiently for the field emission and thermionic field emission to dominate the current flow. The ohmic behavior presented by the ZnO1-PtIr contact suggests that the charge transport mechanism is based on carrier tunneling through a thin barrier.

Figure 14 – (a) c-AFM scheme; I-V characteristics of grain and grain boundary for (b) ZnO1, (c) ZnO4, and (d) ZnO8. Insets: A semi-log plot of forward bias I-V characteristics obtained from grain and grain boundary.

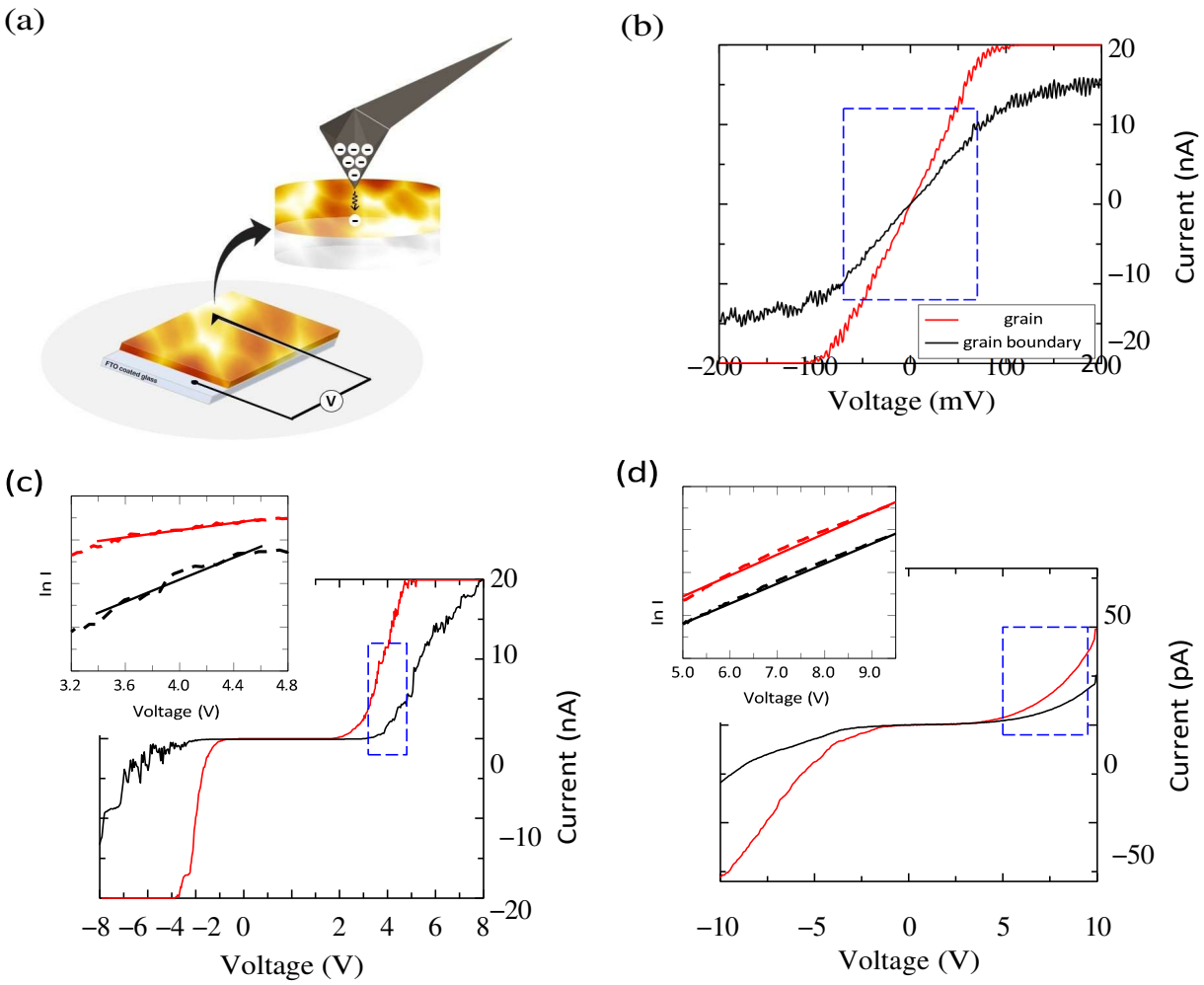

Source: Author.

3.3.3 Energy band diagrams

Figure 15 displays the electron energy band diagram suggested for the n-type ZnO1 before (Fig. 15a) and after the contact (Fig. 15b) with Pt-Ir metal that has a lower work function. Because of the smaller work function, the electrons in the metal are at a higher energy level than the electrons in the Fermi level of the semiconductor, as seen in Fig. 15a. When the materials are brought into contact (Fig. 15b), electrons begin to flow from the metal, owing to its higher energy, to the ZnO conduction band until the Fermi levels (E_F) are aligned. As electrons migrate from the metal to the semiconductor, the concentration of free electrons in the semiconductor region near the boundary increases, while positive charges remain on the metal side. The charge accumulation layer in the semiconductor is confined to a thickness on the order of the Debye length, essentially forming a surface charge. Due to the high concentration of electrons in the

metal, positive charges are also superficial and are contained at a distance of about 0.5 Å from the metal-semiconductor interface. Consequently, there is no formation of a depletion region in the semiconductor, nor a potential barrier for the flow of electrons, either from the semiconductor towards the metal or in the opposite direction (10).

Figure 15 – Energy band diagram of the local contact between the Pt-Ir metal tip and the n-type ZnO1 film with Φm < Φs at the grain and grain boundary regions: (a) before contact, (b) in thermal equilibrium and (c) tunneling process.

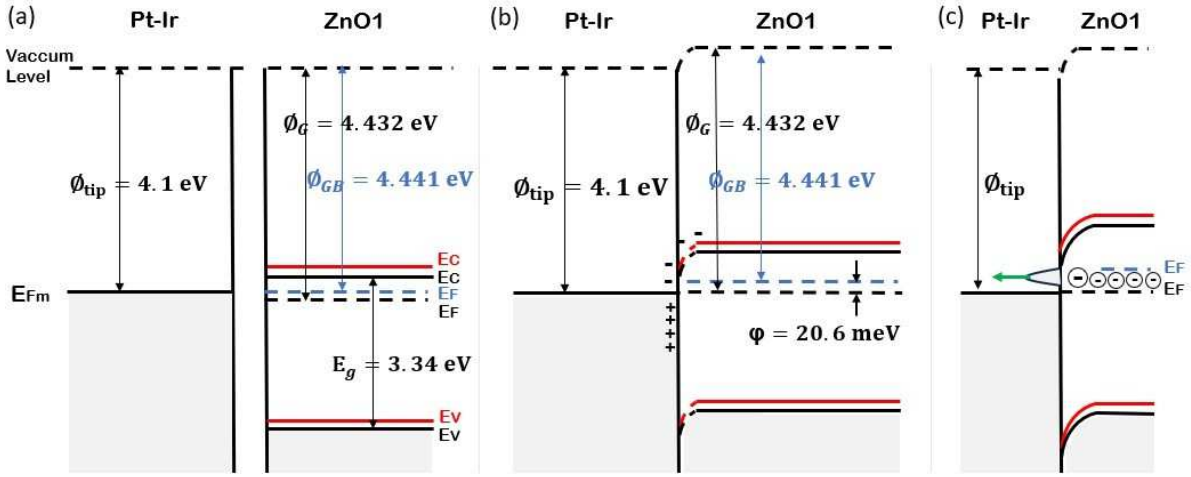

Source: Author.

Furthermore, as the number of electrons in the semiconductor increases, the distance between E_F and the edge of the conduction band (E_C) decreases. However, in thermal equilibrium, E_F remains constant, causing E_C to shift upward parallel to the edge of the valence band (E_V) and the vacuum level. This shift occurs because the semiconductor's optical band gap and electron affinity, defined as the energy difference of an electron between the vacuum level and the lower edge of the conduction band, remain unchanged after contact with the metal.

In a metal-semiconductor system in thermal equilibrium, the vacuum level must maintain continuity through the transition region. Consequently, to ensure continuity, the vacuum level on the semiconductor side must gradually approach the vacuum level on the metal side, resulting in band bending (ϕ). The difference in vacuum levels, equivalent to the difference in work functions, determines the local band curvature (16).

Note that the work functions of the metal and the GB are such that the Fermi levels are aligned before contact with the metal. In the grain region, due to the smaller presence of defect states, E_F moves slightly away from the edge of the conduction band, requiring a small amount of band bending to align the E_F levels (approximately 20.6 meV), forming a thin barrier

of potential between M-S, thin enough so that the dominant conduction process suggested is tunneling, as illustrated in Fig. 15c (91).

Due to the thin depletion region, electrons with energy close to the Fermi level can tunnel from the semiconductor into the metal at low temperatures in a field emission transport process (10). These processes are suggested to explain the electron transport through the M-S ohmic contact observed.

The I-V curves presented in Figs. 14c and 14d demonstrate that the ZnO4 and ZnO8 films, unlike ZnO1, formed rectifying contacts with the Pt-Ir metal, as predicted in KPFM measurements that showed that $\Phi m > \Phi s$ for both films. These contacts suggest the formation of a potential barrier at the M-S interface, indicating that charge transport predominantly occurs through thermionic emission.

According to the thermionic emission theory, the current through the junction barrier as a function of the applied voltage is given by (17, 18):

$$I = I^S \exp\left(-\frac{qV}{nk_BT}\right) - 1 \ , \tag{3.2}$$

where the saturation current I^S depends on the potential barrier according to:

$$I^S \propto \exp\left(-\frac{\Phi}{nk_BT}\right) \ , \tag{3.3}$$

where Φ is the Schottky barrier height (SBH), n is the ideality factor, k_B is the Boltzmann constant and, T is the temperature. According to the TE model, the Schottky diode parameters n and Φ are presumed independent of voltage. These parameters are derived, respectively, from the slope and intercept of the line that best fits the relationship between $\ln I$ and V (insets of Fig. 14c and 14d), expressed as:

$$\ln I = \frac{qV}{nk_BT} + \ln I^S. \tag{3.4}$$

Considering that both grain and GB form similar contacts, the change in potential barrier height $\Delta\Phi$ can be calculated as:

$$\Delta\Phi = nk_BT \ln\left(\frac{I^S_G}{I^S_{GB}}\right) \ , \tag{3.5}$$

where I^S_G and I^S_{GB} are the saturation currents at the grain and the grain boundary(19).

The application of TE model equations, carried out using the mean values of n as 3.60 ± 0.002 and 2.03 ± 0.003 for ZnO4 and ZnO8, respectively, yielded the current values

shown in Table 2. Substituting these values into equation 3.5, variations in the potential barrier height of $\Delta\Phi = 50.41 \pm 0.002$ meV and $\Delta\Phi = 52.54 \pm 0.003$ meV for ZnO1 and ZnO8 were obtained (values displayed in Table 2). At this juncture, it is important to emphasize that the ideality factor *n* indicates the non-ideal behavior exhibited by the Schottky diode. Deviations from ideality can be attributed to the current conduction mechanism under consideration. The TE model, which solely considers the thermionic emission mechanism while disregarding tunneling and recombination processes and the series resistance at the metal-semiconductor junction, results in a higher ideality factor (59).

As discussed, both samples show a noticeable decrease in saturation currents in the grain boundary region. Between samples, the increase in thickness from four to eight layers reduced the saturation current of both grains and GB due to the higher potential barrier formed during M-S contact. However, both samples exhibit the characteristic threshold voltage of Schottky diodes. When forward-biased, conduction through the junction does not begin until the external biasing voltage reaches the "knee voltage," at which point the current increases rapidly. For Schottky diodes, the voltage required for forward conduction is typically around 0.3 to 0.5 volts, with different metal compounds producing varying forward voltage drops. In contrast, for p-n junction diodes such as silicon diodes, the voltage required for forward conduction is around
0.65 to 0.70 volts. This distinction may have advantages for specific applications.

The energy band diagram schemes proposed for ZnO4 and ZnO8 before and after equilibrium is achieved at the local metal-grain interface and metal-grain boundary interface are displayed in Figs. 16 and 17, respectively. According to the Schottky-Mott theory (14, 15), for an n-type semiconductor where $\Phi_M > \Phi_S$, upon bringing the semiconductor into contact with the metal tip, the electrons from the semiconductor's conduction band, which have higher energy than the electrons in the metal (Figs. 16a and 16b for ZnO4, Figs. 17a and 17b for ZnO8), flow into the metal until the Fermi levels align. As electrons transfer from the semiconductor to the metal, the concentration of free electrons near the interface diminishes, leading to a displacement of E_F away from the conduction band edge E_C.

In thermal equilibrium, E_F remains constant, causing E_C to shift upward. The optical gap and electron affinity must remain unchanged after contact, as previously mentioned, and E_V also shifts upward in parallel with E_C along with the vacuum level, which gradually approaches the vacuum level on the metal side, to maintain continuity in the transition region, resulting in band bending.

Figure 16 – Energy band diagram of the local contact between the Pt-Ir metal tip and the n-type ZnO4 film with Φm > Φs at the grain and grain boundary regions: (a) before contact, (b) in thermal equilibrium and (c) thermionic process.

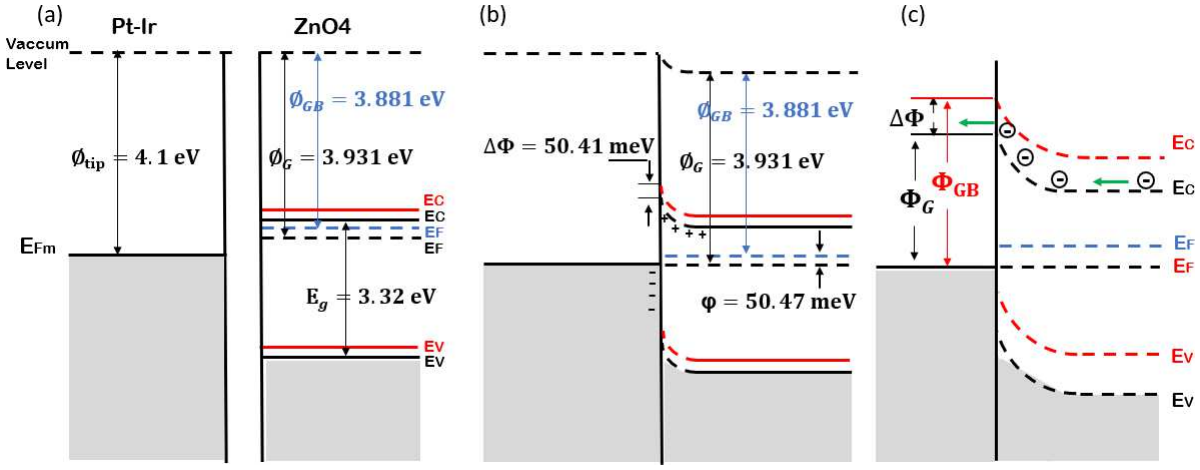

Source: Author.

Figure 17 – Energy band diagram of the local contact between the Pt-Ir metal tip and the n-type ZnO8 film with Φm > Φs at the grain and grain boundary regions: (a) before contact and (b) in thermal equilibrium.

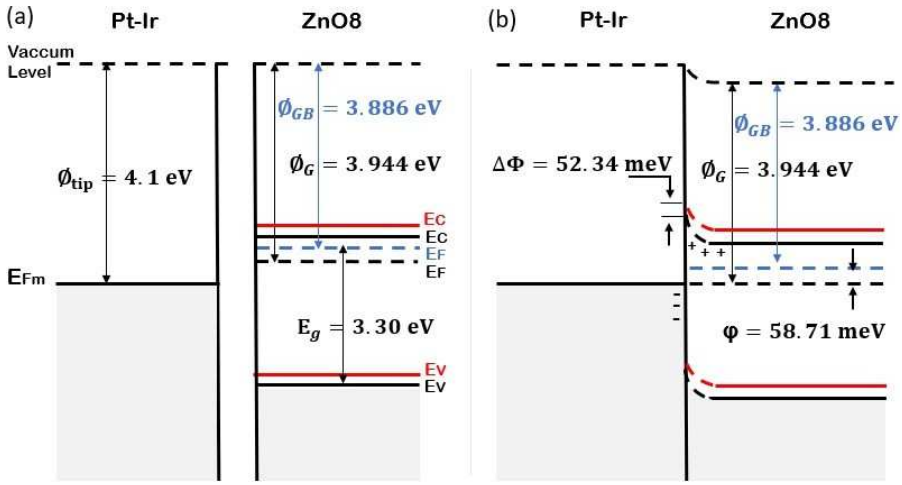

Source: Author.

Notably, the accumulation of defect states within the grain boundaries increases the carrier density and shifts the Fermi levels of both ZnO4 and ZnO8 semiconductors closer to their conduction bands. These shifts reduce GB regions' local work function value, achieving E_F alignment with a substantial band bending. Based on the provided work function values (Φ_{tip}, Φ_G, and Φ_{GB}), the local band bending for ZnO4 and ZnO8 samples was determined and is presented in Table 2. For ZnO4, the band bending at the GB region is approximately $\phi = 50.47$ meV greater than the value at the grain face, consistent with the difference in potential barrier height computed using the thermionic emission theory ($\Delta\Phi = 50.41$ meV). For ZnO8,

the band bending at the GB region is approximately $\phi = 58.71$ meV greater than the value at the grain face, slightly higher than the value computed for the difference in potential barrier height using the thermionic emission theory ($\Delta\Phi = 52.34$ meV). This difference can be justified because the measurement of the work functions by KPFM considers the force applied to neutralize the charges distributed by the film without the semiconductor and the metal tip being brought into direct contact. As the presence of GBs trapped many charges, the resulting value shifted slightly to a higher value.

In a Schottky barrier diode, current flows due to charge transport from the semicon- ductor to the metal or in the reverse direction. An electron emitted over the barrier from the semiconductor into the metal must traverse the high-field depletion region. While traversing this region, drift and diffusion processes govern the electron's motion. However, in the thermionic emission theory, the effect of drift and diffusion in the depletion region is negligible, and the barrier height is assumed to be large compared to $k_B T$. Therefore, only those electrons whose kinetic energy exceeds the height of the potential barrier (as illustrated in Fig. 16c) can reach the top and move towards the metal. Based on established values, this transport mechanism can describe the charge transport through the ZnO4 and ZnO8 films.

3.4 Conclusions

This study investigated the structure and charge transport behavior at the interface between a metal contact and transparent ZnO electrodes, commonly used as optical windows in electrical and optoelectronic devices. It was demonstrated that controlling the film thickness significantly influences the electrical and optical characteristics.

By employing scanning probe microscopy techniques, including EFM, KPFM, and c-AFM modes, the ohmic to Schottky conversion of ZnO/PtIr contacts was observed and modulated by adjusting the number of layers of ZnO films spin-coated on FTO substrates. All films exhibited the formation of grain boundaries to varying degrees during film growth. Topographic and electrical EFM scans revealed the presence of granular structures of various sizes within the samples, along with charge trapping resulting from the defect states associated with these formations. These defects introduced into the band gap, interferes with the Fermi level of ZnO, thereby altering its work function and, consequently, the type of M-S contact formed.

ZnO1 films exhibited excellent conduction properties while maintaining low absorp- tion of visible light with just a single semiconductor layer. In single-layer samples, defect states

resulted in work function values slightly higher than those of the chosen metal. These larger work function values led to the formation of low-resistance contacts, displaying the linear I-V relationship typical of ohmic contacts, along with high local saturation current values. Based on the electrical properties observed, the ohmic behavior of ZnO1 films was attributed to the charge transport mechanism described by field emission theory despite the absence of a potential barrier to charge transfer between the metal and semiconductor. However, grain boundaries slightly shifted the Fermi level of ZnO1, causing minimal band bending (20.6 meV) upon contact with the metal. These properties render one-layer ZnO electrodes excellent candidates for optoelec- tronic devices requiring low contact resistances, minimal light absorption, and transparent or semi-transparent contacts.

ZnO4 and ZnO8 films formed rectifying contacts with the metal, which is attributed to the presence of grain boundaries, which increased in number and size with the thickness of the film. In these samples, accumulated defect states considerably shifted the Fermi level towards the conduction band, reducing the local work function value. Both samples exhibited rectifier behavior, characterized by the I-V relationship and the threshold voltage region typical of a Schottky diode. A potential barrier was formed upon contact with the metal, controlling the charge transport mechanism.

Applying the thermionic emission model equations, which describe the charge transport mechanism across the potential barrier, we obtained the variation in potential barrier height between grains and grain boundaries for both samples. Upon contact with the metal, the alignment of the Fermi levels of ZnO4, affected by the presence of GBs, necessitated a band bend of approximately 50.47 meV, resulting in a potential barrier height variation of approximately 50.41 meV. In the case of ZnO8, the variation in the potential barrier height caused by the alignment of E_F , approximately 52.34 meV, required a slightly greater degree of band bending (approximately 58.71 meV). The discrepancy in the data for ZnO8 films may have arisen due to limitations in the TE model, which does not account for other simultaneous transport mechanisms and the series resistances present at the interfaces. Despite the deviations, the $\Delta\Phi$ values are consistent with those reported in the literature (17, 19, 92), supporting the suitability of the transport mechanism proposed here.

Furthermore, the ZnO4 films exhibited high saturation current values ($I^S_G = 1.29$ nA and $I^S_{GB} = 0.75$ nA), with a noticeable reduction in current at the GBs due to the accumulation of charges in the region. In ZnO8 films, the slight increase in the potential barrier height significantly

decreased the local saturation current values ($I_G^S = 1.09 \times 10^{-3}$ nA and $I_{GB}^S = 0.40 \times 10^{-3}$ nA). Additionally, a slight shift in the threshold voltage of ZnO8 towards larger values was observed, highlighting the potential of thicker films as surge suppressors (18, 93), which are electrical devices featuring a nonlinear current-voltage relationship used to limit voltage transients in transmission lines and electronic circuits.

This study is anticipated to contribute to understanding the potential charge transport mechanisms across M-S interfaces and how synthesis parameters such as film thickness influence the charge transport properties. Moreover, it is essential to emphasize the possibility of obtaining high-quality thin films using minimal material through simple deposition techniques such as spin coating.

4 CONCLUSIONS AND FUTURE WORK

This thesis explored the structure and charge transport behavior at the interface between a metal contact and transparent ZnO electrodes, commonly employed as optical windows in electrical and optoelectronic devices. It was demonstrated that controlling the film thickness significantly impacts the electrical and optical characteristics.

Initially, synthesizing a four-layer ZnO film revealed the presence of grain boundaries on films grown on a conductive substrate and their impact on current and potential barriers at the nanoscale. Topographic images and electrostatic force microscopy (EFM) measurements confirmed the presence of grain boundaries and charge trapping in the region. The presence of defect states, resulting in charge confinement and controlling transport through the film, was numerically indicated by the Urbach energy (0.236 eV). In an FTO/ZnO/Pt-Ir structure, the formation of a Schottky-type junction between the semiconductor ZnO and Pt-coated tip was evident. Measurements of the variation of the Kelvin probe force microscopy (KPFM) surface potential confirmed the formation of the Schottky junction based on the work function values obtained (Φ_G = 3.93 eV and Φ_{GB} = 3.89 eV). Local I-V curves obtained from conductive atomic force microscopy (c-AFM) measurements at various randomly chosen locations confirmed band bending in the grain boundaries. The local current values in the grains ($I^G = 1.29 \pm 0.2$ nA) and grain boundaries ($I^{GB} = 0.75 \pm 0.2$ nA), along with the variation in the potential barrier between the grain and grain boundary ($\Delta\Phi = 40.4 \pm 0.2$ meV), indicate that band bending and the variation in surface potential at grain boundaries directly affect charge transport in the films. Subsequently, employing the same scanning probe microscopy techniques, including EFM, KPFM, and c-AFM modes, the ohmic to Schottky conversion of ZnO/PtIr contacts was observed and modulated by adjusting the number of layers of ZnO films spin-coated on FTO substrates. All films exhibited the formation of grain boundaries to varying degrees during film growth. Topographic and electrical EFM scans revealed the presence of granular structures of various sizes within the samples, along with charge trapping resulting from the defect states associated with these formations. These defects introduced optically active states into the band gap, interfering with the Fermi level of ZnO, thereby altering its work function and, consequently, the type of M-S contact formed.

ZnO1 films exhibited excellent conduction properties while maintaining low absorp- tion of visible light with just a single semiconductor layer. In single-layer samples, defect states resulted in work function values slightly higher than those of the chosen metal. These larger work function values led to the formation of low-resistance contacts, displaying the linear I-V relationship typical of ohmic contacts, along with high local saturation current values. Based on the electrical properties observed, the ohmic behavior of ZnO1 films was attributed to the charge transport mechanism described by field emission theory despite the absence of a potential barrier to charge transfer between the metal

and semiconductor. However, grain boundaries slightly shifted the Fermi level of ZnO1, causing minimal band bending (20.6 meV) upon contact with the metal. These properties render one-layer ZnO electrodes excellent candidates for optoelec- tronic devices requiring low contact resistances, minimal light absorption, and transparent or semi-transparent contacts.

ZnO4 and ZnO8 films formed rectifying contacts with the metal, which is attributed to the presence of grain boundaries, which increased in number and size with the thickness of the film. In these samples, accumulated defect states considerably shifted the Fermi level towards the conduction band, reducing the local work function value. Both samples exhibited rectifier behavior, characterized by the I-V relationship and the threshold voltage region typical of a Schottky diode. A potential barrier was formed upon contact with the metal, controlling the charge transport mechanism.

Applying the thermionic emission model equations, which describe the charge transport mechanism across the potential barrier, we obtained the variation in potential barrier height between grains and grain boundaries for both samples. Upon contact with the metal, the alignment of the Fermi levels of ZnO4, affected by the presence of GBs, necessitated a band bend of approximately 50.47meV, resulting in a potential barrier height variation of approximately 50.41meV. In the case of ZnO8, the variation in the potential barrier height caused by the alignment of E_F, approximately 52.34meV, required a slightly greater degree of band bending (approximately 58.71meV). The discrepancy in the data for ZnO8 films may have arisen due to limitations in the TE model, which does not account for other simultaneous transport mechanisms and the series resistances present at the interfaces. Despite the deviations, the $\Delta\Phi$ values are consistent with those reported in the literature (17, 19, 92), supporting the suitability of the transport mechanism proposed here.

Furthermore, the ZnO4 films exhibited high saturation current values ($I_G^S = 1.29$ nA and $I_{GB}^S = 0.75$ nA), with a noticeable reduction in current at the grain boundaries due to the accumulation of charges in the region. In ZnO8 films, the slight increase in the potential barrier height significantly decreased the local saturation current values ($I_G^S = 1.09\times10^{-3}$ nA and $I_{GB}^S = 0.40 \times 10^{-3}$ nA). Additionally, a slight shift in the threshold voltage of ZnO8 towards larger values was observed, highlighting the potential of thicker films as surge suppressors (18, 93), which are electrical devices featuring a nonlinear current-voltage relationship used to limit voltage transients in transmission lines and electronic circuits.

This study is anticipated to contribute to understanding the potential charge transport mechanisms across M-S interfaces and how synthesis parameters such as film thickness influence the charge transport properties. Moreover, it is essential to emphasize the possibility of obtaining high-quality thin films using minimal material through simple deposition techniques such as spin coating.

4.1 Future Work

As an essential component for many emerging technologies, transparent semicon- ductors remain an area ripe for investigation across various domains, including morphological, structural, optoelectronic, electrical, and charge transport properties. It is suggested that zinc oxide be doped with other metals, such as rare earth metals, owing to their excellent thermal and electrical conduction properties. The proposed approach involves synthesizing zinc oxide nanoparticles, preferably utilizing simple techniques that demand minimal time and materials; preparing dispersions using solvents suitable for depositing films onto conductive substrates (ei- ther rigid or flexible); exploring film deposition parameters employing the spin coating technique; conducting morphological, structural, and electrical characterization studies; and innovatively investigating the photoluminescent properties of these materials and their impact on charge transport properties across interfaces formed with metals or other semiconductors.

REFERENCES

1 ROGHABADI, F. A.; AHMADI, N.; AHMADI, V.; CARLO, A.; AGHMIUNI, K. O.; TEHRANI, A. S.; GHOREISHI, F. S.; PAYANDEH, M.; FUMANI, N. M. R. Bulk heterojunction polymer solar cell and perovskite solar cell: concepts, materials, current status, and opto-electronic properties. **Solar Energy**, [S.L.], v. 173, p. 407–424, oct. 2018. Elsevier BV.

2 JIAO, L.; MEI, Y.; XU, D.; ZHONG, S.; MA, J.; ZHANG, L.; BAO, L. Microstructural and electrical characteristics of rare earth oxides doped ZnO varistor films. **J. Appl. Phys.**, [S.L.], v. 123, n. 6, 13 fev. 2018. AIP Publishing. Available at: http://dx.doi.org/10.1063/1.5016085. Accessed at: 12 apr. 2023.

3 CHEN, S.; MANDERS, J. R.; TSANG, S.-W.; SO, F. Metal oxides for interface engineering in polymer solar cells. **J. Mater. Chem.**, [S.L.], v. 22, n. 46, p. 24202–24212, 2012. Royal Society of Chemistry (RSC).

4 MANSOUR, S. A.; YAKUPHANOGLU, F. Electrical-optical properties of nanofiber ZnO film grown by sol-gel method and fabrication of ZnO/p-Si heterojunction. **Solid State Sci.**, [S.L.], v. 14, n. 1, p. 121-126, jan. 2012. Elsevier BV.

5 KUO, F.-L.; LI, Y.; SOLOMON, M.; DU, J.; SHEPHERD, N. D. Workfunction tuning of zinc oxide films by argon sputtering and oxygen plasma: An experimental and computational study. **Journal Of Physics D**: Applied Physics, [S.L.], v. 45, n. 6, p. 065301, 27 jan. 2012. IOP Publishing. Available at: http://dx.doi.org/10.1088/0022-3727/45/6/065301. Accessed at: 09 apr. 2023.

6 COPPA, B. J.; DAVIS, R. F.; NEMANICH, R. J. Gold Schottky contacts on oxygen plasma-treated, n-type ZnO($000\bar{1}$). **Appl. Phys. Lett.**, [S.L.], v. 82, n. 3, p. 400-402, 20 jan. 2003. AIP Publishing.

7 HU, T.; LI, F.; YUAN, K.; CHEN, Y. Efficiency and air-stability improvement of flexible inverted polymer solar cells using ZnO/poly(ethylene glycol) hybrids as cathode buffer layers. **ACS Appl. Mater. Inter.**, [S.L.], v. 5, n. 12, p. 5763-5770, 14 jun. 2013. American Chemical Society (ACS).

8 TÜZEMEN, E. S.; EKER, S.; KAVAK, H.; ESEN, R. Dependence of film thickness on the structural and optical properties of ZnO thin films. **Appl. Surf. Sci.**, [S.L.], v. 255, n. 12, p. 6195-6200, apr. 2009. Elsevier BV.

9 SU, L.; GUAN, Z.; LIU, Q.; ZHU, Y. Ohmic-Schottky conversion of ZnO/metal contact modulated by a plasma surface treatment method. **Results Mater.**, [S.L.], v. 15, p. 100290, sep. 2022. Elsevier BV. Available at: http://dx.doi.org/10.1016/j.rinma.2022.100290. Accessed at: 20 apr. 2023.

10 TYAGI, M. S.. Physics of Schottky Barrier Junctions. **Metal-Semiconductor Schottky Barrier Junctions And Their Applications**, [S.L.], p. 1-60, 1984. Springer US.

11 REYES, P. I.; KU, C.-J.; DUAN, Z.; XU, Y.; GARFUNKEL, E.; LU, Y. Reduction of persistent photoconductivity in ZnO thin film transistor-based UV photodetector. **Appl. Phys. Lett.**, [S.L.], v. 101, n. 3, 16 jul. 2012. AIP Publishing. Available at: http://dx.doi.org/10.1063/1.4737648. Accessed at: 10 nov. 2022

12 SU, L.; ZHU, Y.; XU, X.; CHEN, H.; TANG, Z.; FANG, X. Back-to-back symmetric Schottky type UVA photodetector based on ternary alloy BeZnO. **J. Mater. Chem. C**, v. 6, n. 29,
p. 7776–7782, 2018.

13 HWANG, J.-D.; HONG, Z.-J. Enhancing the Schottky-barrier height by inserting a thin MgO layer between Au and annealed-ZnO. **Mater. Res. Bull.**, [S.L.], v. 144, p. 111478, dec. 2021. Elsevier BV. Available at: http://dx.doi.org/10.1016/j.materresbull.2021.111478. Accessed at: 10 nov. 2022.

14 SCHOTTKY, W. Halbleitertheorie der sperrschicht. **Die Naturwissenschaften**, [S.L.], v. 26, n. 52, p. 843-843, dec. 1938. Springer Science and Business Media LLC.

15 MOTT, N. F. Note on the contact between a metal and an insulator or semi-conductor. **Math. Proc. Camb. Philos. Soc.**, [S.L.], v. 34, n. 4, p. 568-572, oct. 1938. Cambridge University Press (CUP).

16 GRZADZIEL, L.; KRZYWIECKI, M.; SZWAJCA, A.; SARFRAZ, A.; GENCHEV, G.; ERBE, A. Detection of intra-band gap defects states in spin-coated sol-gel SnO_x nanolayers by photoelectron spectroscopies. **J. Phys. D Appl. Phys.**, [S.L.], v. 51, n. 31, p. 315301, 11 jul. 2018. IOP Publishing. Available at: http://dx.doi.org/10.1088/1361-6463/aacf3a. Accessed at: 1 dec. 2023.

17 KUMAR, M.; BASU, T.; SOM, T. Local probe microscopic studies on Al-doped ZnO: Pseudoferroelectricity and band bending at grain boundaries. **J. Appl. Phys.**, [S.L.], v. 119, n. 1, 7 jan. 2016. AIP Publishing. Available at: http://dx.doi.org/10.1063/1.4939559. Accessed at: 17 mar. 2023.

18 SAADELDIN, M. M.; DESOUKY, O. A.; IBRAHIM, M.; KHALIL, G. E.; HELALI, M. Y. Investigation of structural and electrical properties of ZnO varistor samples doped with different additives. **NRIAG J. Astron. Geophys.**, [S.L.], v. 7, n. 2, p. 201-207, dec. 2018. Informa UK Limited.

19 SINGH, R.; SOM, T. Direct evidence of band-bending at grain boundaries of ZnO:SnO_2 films: Local probe microscopic studies. **Sol. Energy**, [S.L.], v. 208, p. 275-281, sep. 2020. Elsevier BV.

20 FRANKENSTEIN, H.; LENG, C. Z.; LOSEGO, M. D.; FREY, G. L. Atomic layer deposition of ZnO electron transporting layers directly onto the active layer of organic solar cells. **Org. Electron.**, [S.L.], v. 64, p. 37-46, jan. 2019. Elsevier BV.

21 YU, C.-F.; CHEN, S.-H.; XIE, W.-J.; LIN, Y.-S.; SHEN, C.-Y.; TSAI, S.-J.; SUNG, C.-W.; AY, C. Nanoscale surface electrical properties of zinc oxide films investigated by conducting atomic force microscopy. **Microsc. Res. Techniq.**, [S.L.], v. 71, n. 1, p. 1-4, 28 aug. 2007. Wiley.

22 ZHAO, X.; HEPING, S.; YE, Z.; XIN, L.; XIAOCHONG, Z.; MEIQIAN, T.; JINGFENG, L.; JIANBAO, L.; HONG, L. Aluminum-doped zinc oxide as highly stable electron collection layer for perovskite solar cells. **ACS Appl. Mater. Interfaces**, [S.L.], v. 8, n. 12, p. 7826-7833, 18 mar. 2016. American Chemical Society (ACS).

23 ONGUL, F. Solution-processed inverted organic solar cell using V_2O_5 hole transport layer and vacuum free EGaIn anode. **Opt. Mater.**, [S.L.], v. 50, p. 244-249, dec. 2015. Elsevier BV.

24 SAHDAN, M. Z.; MALEK, M. F.; ALIAS, M. S.; KAMARUDDIN, S. A.; NORHIDAYAH, C. A.; SARIP, N.; NAFARIZAL, N.; RUSOP, M. Fabrication of inverted bulk heterojunction organic solar cells based on conjugated P3HT:PCBM using various thicknesses of ZnO buffer layer. **Optik**, [S.L.], v. 126, n. 6, p. 645-648, mar. 2015. Elsevier BV.

25 AHMAD, S.; ABBAS, H.; KHAN, M. B.; NAGAL, V.; HAFIZ, A.; KHAN, Z. H. ZnO for stable and efficient perovskite bulk heterojunction solar cell fabricated under ambient atmosphere. **Sol. Energy**, [S.L.], v. 216, p. 164-170, mar. 2021. Elsevier BV.

26 MAMMAH, S. L.; OPARA, F. E.; SIGALO, F. B.; EZUGWU, S. C.; EZEMA, F.

I. *et al.* Effect of concentration on the optical and solid state properties of ZnO thin films deposited by aqueous chemical growth (ACG) method. **J. Mod. Phys.**, [S.L.], v. 03, n. 10, p. 1516-1522, 2012. Scientific Research Publishing, Inc.

27 LI, Z.; YAN, T.; FANG, X. Low-dimensional wide-bandgap semiconductors for UV photodetectors. **Nat. Rev. Mater.**, [S.L.], v. 8, n. 9, p. 587-603, 18 aug. 2023. Springer Science and Business Media LLC.

28 CHEN, Y.; SU, L.; JIANG, M.; FANG, X. Switch type PANI/ZnO core-shell microwire heterojunction for UV photodetection. **J. Mater. Sci. Technol.**, [S.L.], v. 105, p. 259-265, apr. 2022. Elsevier BV.

29 ZHAO, B.; WANG, F.; CHEN, H.; ZHENG, L.; SU, L.; ZHAO, D.; FANG, X. An ultrahigh responsivity (9.7 mA W^{-1}) self-powered solar-blind photodetector based on individual ZnO-Ga_2O_3 heterostructures. **Adv. Funct. Mater.**, [S.L.], v. 27, n. 17, 22 mar. 2017. Wiley. Available at: http://dx.doi.org/10.1002/adfm.201700264. Accessed at: 20 jul. 2023.

30 ÖZGÜR, U.; ALIVOV, Y. I.; LIU, C.; TEKE, A.; RESHCHIKOV, M. A.; DOĞAN, S.; AVRUTIN, V.; CHO, S.-J.; MORKOÇ, H. A comprehensive review of ZnO materials and devices. **J. Appl. Phys.**, [S.L.], v. 98, n. 4, p. 1-1, 15 ago. 2005. AIP Publishing. Available at: http://dx.doi.org/10.1063/1.1992666. Accessed at: 10 jan. 2021.

31 SUN, Y.; SEO, J. H.; TAKACS, C. J.; SEIFTER, J.; HEEGER, A. J. Inverted polymer solar cells integrated with a low-temperature-annealed sol-gel-derived ZnO film as an electron transport layer. **Adv. Mater.**, [S.L.], v. 23, n. 14, p. 1679-1683, 22 feb. 2011. Wiley.

32 KREBS, F. C.; THOMANN, Y.; THOMANN, R.; ANDREASEN, J. W. A simple nanostructured polymer/ZnO hybrid solar cell preparation and operation in air. **Nanotechnology**, [S.L.], v. 19, n. 42, p. 424013, 25 sep. 2008. IOP Publishing. Available at: http://dx.doi.org/10.1088/0957-4484/19/42/424013. Accessed at: 1 jan. 2021.

33 GUPTA, D.; DUTTA, D.; KUMAR, M.; BARMAN, P. B.; SOM, T.; HAZRA, S. K. Temperature dependent dual hydrogen sensor response of Pd nanoparticle decorated Al-doped ZnO surfaces. **J. Appl. Phys.**, [S.L.], v. 118, n. 16, 22 out. 2015. AIP Publishing. Available at: http://dx.doi.org/10.1063/1.4934521. Accessed at: 5 jul. 2023.

34 BAIER, R.; LEENDERTZ, C.; ABOU-RAS, D.; LUX-STEINER, M. C.; SADEWASSER, S. Properties of electronic potential barriers at grain boundaries in Cu(In,Ga)Se_2 thin films. **Sol. Energy Mater. Sol. Cells**, [S.L.], v. 130, p. 124-131, nov. 2014. Elsevier BV.

35 CONSONNI, V.; BAIER, N.; ROBACH, O.; CAYRON, C.; DONATINI, F.; FEUILLET, G. Local band bending and grain-to-grain interaction induced strain nonuniformity in polycrystalline CdTe films. **Phys. Rev. B**, [S.L.], v. 89, n. 3, p. 035310, 21 jan. 2014. American Physical Society (APS). Available at: http://dx.doi.org/10.1103/physrevb.89.035310. Accessed at: 27 jul. 2023.

36 JACKSON, P.; HARISKOS, D.; LOTTER, E.; PAETEL, S.; WUERZ, R.; MENNER, R.; WISCHMANN, W.; POWALLA, M. New world record efficiency for Cu(In,Ga)Se_2 thin-film solar cells beyond 20%. **Prog. Photovolt.: Res. Appl.**, [S.L.], v. 19, n. 7, p. 894-897, 5 jan. 2011. Wiley.

37 AZULAY, D.; BALBERG, I.; MILLO, O. Microscopic evidence for the modification of the electronic structure at grain boundaries of ZnO. **Phys. Rev. Lett.**, [S.L.], v. 108, n. 7, p. 1–2, 14 feb. 2012. American Physical Society (APS).

38 JI, X.; ZHU, Y.; CHEN, M.; SU, L.; CHEN, A.; GUI, X.; XIANG, R.; TANG, Z. The modulation of grain boundary barrier in ZnMgO/ZnO heterostructure by surface polar liquid. **Sci. Rep.**, [S.L.], v. 4, n. 1, p. 1–2, 25 feb. 2014. Springer Science and Business Media LLC.

39 LIKOVICH, E. M.; JARAMILLO, R.; RUSSELL, K. J.; RAMANATHAN, S.;

NARAYANAMURTI, V. Narrow band defect luminescence from Al-doped ZnO probed by scanning tunneling cathodoluminescence. **Appl. Phys. Lett.**, [S.L.], v. 99, n. 15, p. 151910, 10 oct. 2011. AIP Publishing. Available at: http://dx.doi.org/10.1063/1.3647622. Accessed at: 11 aug. 2023.

40 BIKOWSKI, A.; ELLMER, K. A comparative study of electronic and structural properties of polycrystalline and epitaxial magnetron-sputtered ZnO: Al and $Zn_{1-x}Mg_xO$. **J. Appl. Phys.**, [S.L.], v. 114, n. 6, p. 063709, 9 ago. 2013. AIP Publishing. Available at: http://dx.doi.org/10.1063/1.4817376. Accessed at: 5 nov. 2023.

41 MEYER, E.; HUG, H. J.; BENNEWITZ, R. **Scanning probe microscopy:** The lab on a tip. Berlin: Springer, 2004. 322 p.

42 SHARMA, A.; UNTCH, M.; QUINTON, J. S.; BERGER, R.; ANDERSSON, G.; LEWIS, D. A. Nanoscale heterogeneity and workfunction variations in ZnO thin films. **Appl. Surf. Sci.**,
[S.L.], v. 363, p. 516-521, feb. 2016. Elsevier BV.

43 BEEK, W. J. E.; WIENK, M. M.; KEMERINK, M.; YANG, X.; JANSSEN, R. A. J. Hybrid zinc oxide conjugated polymer bulk heterojunction solar cells. **J. Phys. Chem. B**, [S.L.], v. 109, n. 19, p. 9505-9516, 9 apr. 2005. American Chemical Society (ACS).

44 PACHOLSKI, C.; KORNOWSKI, A.; WELLER, H. Self-assembly of ZnO: from nanodots to nanorods. **Angew. Chem. Int. Ed.**, v. 41, n. 7, p. 1188–1191, 2002.

45 SAGHEER, R.; KHALIL, M.; ABBAS, V.; KAYANI, Z. N.; TARIQ, U.; ASHRAF, F. Effect of Mg doping on structural, morphological, optical and thermal properties of ZnO nanoparticles. **Optik**, [S.L.], v. 200, p. 163428, jan. 2020. Elsevier BV. Available at: http://dx.doi.org/10.1016/j.ijleo.2019.163428. Accessed at: 10 jul. 2021.

46 APRILIA, A.; WULANDARI, P.; SUENDO, V.; HERMAN; HIDAYAT, R.; FUJII, A.; OZAKI, M. Influences of dopant concentration in sol–gel derived AZO layer on the performance of P3HT:PCBM based inverted solar cell. **Sol. Energy Mater. Sol. Cells**, [S.L.], v. 111, p. 181-188, abr. 2013. Elsevier BV.

47 RUCAVADO, E.; JEANGROS, Q.; URBAN, D. F.; HOLOVSKÝ, J.; REMES, Z.; DUCHAMP, M.; LANDUCCI, F.; DUNIN-BORKOWSKI, R. E.; KÖRNER, W.; ELSÄSSER, C.; HESSLER-WYSER, A.; MORALES-MASIS, M.; BALLIF, C. Enhancing the optoelectronic properties of amorphous zinc tin oxide by subgap defect passivation: a theoretical and experimental demonstration. **Phys. Rev. B**, [S.L.], v. 95, n. 24, p. 24520, 9 jun. 2017. American Physical Society (APS). Available at: http://dx.doi.org/10.1103/physrevb.95.245204. Accessed at: 6 sep. 2023.

48 SCARMINIO, J.; URBANO, A.; GARDES, B. The Beer-Lambert law for electrochromic tungsten oxide thin films. **Mater. Chem. Phys.**, [S.L.], v. 61, n. 2, p. 143-146, oct. 1999. Elsevier BV.

49 SINGH, R.; DUTTA, A.; NANDI, P.; SRIVASTAVA, S. K.; SOM, T. Influence of grain size on local work function and optoelectronic properties of n-ZTO/p-Si heterostructures. **Appl. Surf. Sci.**, [S.L.], v. 493, p. 577-586, nov. 2019. Elsevier BV.

50 MANDAL, S. K.; NATH, T. K.; DAS, A. Reduction of magnetization in $Zn_{0.9}Fe_{0.1}O$ diluted magnetic semiconducting nanoparticles by doping of Co or Mn ions. **J. Appl. Phys.**, [S.L.], v. 101, n. 12, p. 123920, 15 jun. 2007. AIP Publishing. Available at: http://dx.doi.org/10.1063/1.2748614. Accessed at: 8 dec. 2023.

51 PEREIRA, M. S.; LIMA, F. A. S.; SILVA, C. B.; FREIRE, P. T. C.; VASCONCELOS, I. F. Structural, morphological, and optical properties of SnO_2 nanoparticles obtained by a proteic sol–gel method and their application in dye-sensitized solar cells. **J. Sol-Gel Sci. Technol.**, [S.L.], v. 84, n. 1, p. 206-213, 22 aug. 2017. Springer Science and

Business Media LLC.

52 SWALLOW, J. E. N.; WILLIAMSON, B. A. D.; WHITTLES, T. J.; BIRKETT, M.; FEATHERSTONE, T. J.; PENG, N.; ABBOTT, A.; FARNWORTH, M.; CHEETHAM, K. J.; WARREN, P.; SCANLON, D. O.; DHANAK, V. R.; VEAL, T. D. Self-compensation in transparent conducting F-doped SnO_2. **Adv. Funct. Mater.**, [S.L.], v. 28, n. 4, p. 1701900, 27 nov. 2017. Wiley. Available at: http://dx.doi.org/10.1002/adfm.201701900. Accessed at: 16 jan. 2024.

53 FARAJ, M. G.; AHMED, D. R. Photoelectrochemical study of zinc oxide (ZnO) thin films on different polymer substrates by sputtering technique. **Indian J. Phys.**, [S.L.], v. 98, n. 6, p. 1965-1968, 28 sep. 2023. Springer Science and Business Media LLC.

54 ŞENAY, V.; PAT, S.; KORKMAZ, Ş.; AYDOĞMUŞ, T.; ELMAS, S.; ÖZEN, S.; EKEM, N.; BALBAĞ, M. Z. ZnO thin film synthesis by reactive radio frequency magnetron sputtering. **Appl. Surf. Sci.**, [S.L.], v. 318, p. 2-5, nov. 2014. Elsevier BV.

55 EKEM, N.; KORKMAZ, S.; PAT, S.; BALBAG, M.; CETIN, E.; OZMUMCU, M. Some physical properties of ZnO thin films prepared by RF sputtering technique. **Int. J. Hydrogen Energy**, [S.L.], v. 34, n. 12, p. 5218-5222, jun. 2009. Elsevier BV.

56 FONOBEROV, V. A.; ALIM, K. A.; BALANDIN, A. A.; XIU, F.; LIU, J. Photoluminescence investigation of the carrier recombination processes in ZnO quantum dots and nanocrystals. **Phys. Rev. B**, [S.L.], v. 73, n. 16, p. 1, 17 apr. 2006. American Physical Society (APS). Available at: http://dx.doi.org/10.1103/physrevb.73.165317. Accessed at: 20 dec. 2023.

57 LIN, K.-F.; CHENG, H.-M.; HSU, H.-C.; LIN, L.-J.; HSIEH, W.-F. Band gap variation ofsize-controlled ZnO quantum dots synthesized by sol-gel method. **Chem. Phys. Lett.**, [S.L.], v. 409, n. 4-6, p. 208-211, jun. 2005. Elsevier BV.

58 PARK, J.; RIM, Y. S.; SENANAYAKE, P.; WU, J.; STREIT, D. Electrical defect state distribution in single crystal ZnO Schottky barrier diodes. **Coatings**, [S.L.], v. 10, n. 3, p. 206, 27 feb. 2020. MDPI AG.

59 CHAITRA, U.; ALI, A. V. M.; MAHESHA, M. G.; KOMPA, A.; KEKUDA, D.; RAO, K. M. Property evaluation of spin-coated Al-doped ZnO thin films and Au/AZO/FTO Schottky diodes. **Superlattices Microstruct.**, [S.L.], v. 155, p. 106903, jul. 2021. Elsevier BV. Available at: http://dx.doi.org/10.1016/j.spmi.2021.106903. Accessed at: 25 nov. 2023.

60 KHAMIS, F.; ZAGGOUT, F.; DEGIG, N. Optical properties of pure zinc oxide thin films prepared by sol-gel method. **Al-Satil**, [S.L.], v. 14, p. 1–13, 2020.

61 NOROUZZADEH, P.; MABHOUTI, K.; GOLZAN, M. M.; NADERALI, R. Investigation of structural, morphological and optical characteristics of Mn substituted Al-doped ZnO NPs: A Urbach energy and Kramers-Kronig study. **Optik**, [S.L.], v. 204, p. 164227, fev. 2020. Elsevier BV. Available at: http://dx.doi.org/10.1016/j.ijleo.2020.164227. Accessed at: 20 mar. 2023.

62 ALJAAFARI, A.; AHMED, F.; AWADA, C.; SHAALAN, N. M. Flower-like ZnO nanorods synthesized by microwave-assisted one-pot method for detecting reducing gases: structural properties and sensing reversibility. **Front. Chem.**, [S.L.], v. 8, p. 456, 2 jul. 2020. Frontiers Media SA.

63 ALLEJA, J. M.; CARDONA, M. Resonant Raman scattering in ZnO. **Phys. Rev. B**, [S.L.], v. 16, n. 8, p. 3753-3761, 15 oct. 1977. American Physical Society (APS).

64 ŠĆEPANOVIĆ, M.; GRUJIĆ-BROJĞIN, M.; VOJISAVLJEVIĆ, K.; BERNIK, S.; SREĆKOVIĆ, T. Raman study of structural disorder in ZnO nanopowders. **J. Raman Spectrosc.**, [S.L.], v. 41, n. 9, p. 914-921, 18 nov. 2009. Wiley.

65 GHENO, S. M.; HASEGAWA, H. L.; Paulin Filho, P. I. Direct probing of semiconductor barium titanate via electrostatic force microscopy. **Ceramica**, [S.L.], v. 53, n. 326, p. 200-204, jun. 2007. FapUNIFESP (SciELO).

66 WU, W.; HORIBE, Y.; LEE, N.; CHEONG, S.-W.; GUEST, J. R. Conduction of topologically protected charged ferroelectric domain walls. **Phys. Rev. Lett.**, [S.L.], v. 108, n. 7, p. 077203, 14 fev. 2012. American Physical Society (APS). Available at: http://dx.doi.org/10.1103/physrevlett.108.077203. Accessed at: 29 nov. 2023.

67 NANDY, S.; GONÇALVES, G.; PINTO, J. V.; BUSANI, T.; FIGUEIREDO, V.; PEREIRA, L.; MARTINS, R. F. P.; FORTUNATO, E. Current transport mechanism at metal-semiconductor nanoscale interfaces based on ultrahigh density arrays of p-type NiO nano-pillars. **Nanoscale**, [S.L.], v. 5, n. 23, p. 11699, 2013. Royal Society of Chemistry (RSC). Available at: http://dx.doi.org/10.1039/c3nr03803c. Accessed at: 20 oct. 2023.

68 IONESCU-ZANETTI, C.; MECHLER, A.; CARTER, S. A.; LAL, R. Semiconductive polymer blends: correlating structure with transport properties at the nanoscale. **Adv. Mater.**, [S.L.], v. 16, n. 5, p. 385-389, 5 mar. 2004. Wiley.

69 MCCLUSKEY, M. D.; JOKELA, S. J. Defects in ZnO. **J. Appl. Phys.**, [S.L.], v. 106, n. 7, 1 oct. 2009. AIP Publishing. Available at: http://dx.doi.org/10.1063/1.3216464. Accessed at: 30 mar. 2023.

70 UKLEIN, A. V.; MULTIAN, V. V.; KUZ'MICHEVA, G. M.; LINNIK, R. P.; LISNYAK, V. V.; POPOV, A. I.; GAYVORONSKY, V. Y. Nonlinear optical response of bulk ZnO crystals with different content of intrinsic defects. **Opt. Mater.**, [S.L.], v. 84, p. 738-747, oct. 2018. Elsevier BV.

71 BERGMANN, V. W.; WEBER, S. A. L.; RAMOS, F. J.; NAZEERUDDIN, M. K.; GRÄTZEL, M.; LI, D.; DOMANSKI, A. L.; LIEBERWIRTH, I.; AHMAD, S.; BERGER, R. Real-space observation of unbalanced charge distribution inside a perovskite-sensitized solar cell. **Nat. Commun.**, [S.L.], v. 5, n. 1, p. 1, 22 sep. 2014. Springer Science and Business Media LLC.

72 VENKATESAN, S.; NGO, E.; KHATIWADA, D.; ZHANG, C.; QIAO, Q. Enhanced lifetime of polymer solar cells by surface passivation of metal oxide buffer layers. **ACS Appl. Mater. Interfaces**, [S.L.], v. 7, n. 29, p. 16093-16100, 17 jul. 2015. American Chemical Society (ACS).

73 MENSAH-DARKWA, K.; OCAYA, R. O.; AL-SEHEMI, A. G.; YEBOAH, D.; DERE, A.; AL-GHAMDI, A. A.; GUPTA, R. K.; YAKUPHANOĞLU, F. Optoelectronic enhancement of ZnO/p-Si Schottky barrier photodiodes by (Sn, Ti) co-doping. **Phys. B: Condens. Matter.**, [S.L.], v. 667, p. 415155, out. 2023. Elsevier BV. Available at: http://dx.doi.org/10.1016/j.physb.2023.415155. Accessed at: 15 jan. 2024.

74 KIM, H.; JUNG, M. J.; LEE, M. H.; CHOI, B. J. ALD growth of ZnO on GaN: Schottky barrier height engineering using ZnO interlayer. **Mat. Today Comm.**, [S.L.], v. 33, p. 104434, dez. 2022. Elsevier BV. Available at: http://dx.doi.org/10.1016/j.mtcomm.2022.104434. Accessed at: 15 jan. 2024.

75 SINGH, M.; RAJORIYA, M.; SAHNI, M.; GUPTA, P. Effect of aluminum doping on potential barrier of gold-ZnO-Si Schottky barrier diode. **Mat. Today: Proc.**, [S.L.], v. 34, p. 588-592, 2021. Elsevier BV.

76 ZHANG, Y.; ZUO, J.; LI, P.; GAO, Y.; HE, W.; ZHENG, Z. Study of the nanoscale electrical performance of NiO thin films by C-AFM and KPFM techniques: the effect of grain boundary barrier. **Phys. E: Low-Dimens. Syst. Nanostructures**, [S.L.], v. 111, p. 75-78, jul. 2019.

Elsevier BV.

77 LIANG, Q.; QIAO, F.; CUI, X.; HOU, X. Controlling the morphology of ZnO structures via low temperature hydrothermal method and their optoelectronic application. **Mater. Sci. Semicond. Process.**, [S.L.], v. 89, p. 154-160, jan. 2019. Elsevier BV.

78 WANG, N.; WANG, P.; WANG, F.; HE, H.; HUANG, J.; PAN, X.; ZHU, G.; WANG, J.; YE, Z. Improved epitaxy of ZnO films by regulating the layers of graphene. **Appl. Surf. Sci.**,
[S.L.], v. 585, p. 152709, may 2022. Elsevier BV. Available at: http://dx.doi.org/10.1016/j.apsusc.2022.152709. Accessed at: 20 may 2023.

79 HUANG, C.-Y.; LAI, J.-H. Efficient polymer light-emitting diodes with ZnO nanoparticles and interpretation of observed sub-bandgap turn-on phenomenon. **Org. Electron.**, [S.L.], v. 32, p. 244-249, may 2016. Elsevier BV.

80 SUJA, M.; DEBNATH, B.; BASHAR, S. B.; SU, L.; LAKE, R.; LIU, J. Electrically driven plasmon-exciton coupled random lasing in ZnO metal-semiconductor-metal devices. **Appl. Surf. Sci.**, [S.L.], v. 439, p. 525-532, may 2018. Elsevier BV.

81 WANG, Y.-X.; SHEN, Z.-C.; HUANG, D.-D.; YANG, Z.-S. High-performance ZnO nanosheets/nanocrystalline aggregates composite photoanode film in dye-sensitized solar cells. **Mater. Lett.**, [S.L.], v. 214, p. 88-90, mar. 2018. Elsevier BV.

82 AREPALLI, V. K.; LEE, W.-J.; CHUNG, Y.-D.; KIM, J. Growth and device properties of ALD deposited ZnO films for CIGS solar cells. **Mater. Sci. Semicond. Process.**, [S.L.], v. 121, p. 105406, jan. 2021. Elsevier BV. Available at: http://dx.doi.org/10.1016/j.mssp.2020.105406. Accessed at: 15 jan. 2024.

83 MOSBACKER, H. L.; STRZHEMECHNY, Y. M.; WHITE, B. D.; SMITH, P. E.; LOOK, D. C.; REYNOLDS, D. C.; LITTON, C. W.; BRILLSON, L. J. Role of near-surface states in the ohmic-Schottky conversion of Au contacts to ZnO. **Appl. Phys. Lett.**, [S.L.], v. 87, n. 1, 27 jun. 2005. AIP Publishing. Available at: http://dx.doi.org/10.1063/1.1984089. Accessed at: 25 jan. 2024.

84 HERNG, T. S.; KUMAR, A.; ONG, C. S.; FENG, Y. P.; LU, Y. H.; ZENG, K. Y.; DING, J. Investigation of the non-volatile resistance change in noncentrosymmetric compounds. **Sci. Rep.**, [S.L.], v. 2, n. 1, 17 aug. 2012. Springer Science and Business Media LLC. Available at: http://dx.doi.org/10.1038/srep00587. Accessed at: 25 jan. 2024.

85 COPPA, B. J.; FULTON, C. C.; HARTLIEB, P. J.; DAVIS, R. F.; RODRIGUEZ, B. J.; SHIELDS, B. J.; NEMANICH, R. J. In situ cleaning and characterization of oxygen- and zinc-terminated, n-type, ZnO{0001} surfaces. **J. Appl. Phys.**, [S.L.], v. 95, n. 10, p. 5856-5864, 15 may 2004.

86 LI, L.; YAO, C.; DING, B.; XU, N.; SUN, J.; WU, J. Influence of metal covering with a Schottky or ohmic contact on the emission properties of ZnO nanorod arrays. **J. Lumin.**, [S.L.], v. 257, p. 119729, may 2023. Elsevier BV. Available at: http://dx.doi.org/10.1016/j.jlumin.2023.119729. Accesed at: 20 nov. 2023.

87 LIN, Y.-J.; WU, C.-Y.; CHANG, H.-C. Ohmic-rectification conversion that is tuned using H_2O_2 for enhanced rectification and optoelectronic performance in MoS_2/ZnO nanorod devices. **Chin. J. Phys.**, [S.L.], v. 61, p. 22-28, oct. 2019. Elsevier BV.

88 MOREIRA, R.; SANTOS, L. P. M.; SALOMÃO, C.; BARROS, E. B.; VASCONCELOS, I. F. Influence of grain boundaries on nanoscale charge transport properties of transparent conductive ZnO-based electrodes. **ACS Appl. Electron. Mater.**, [S.L.], v. 6, n. 1, p. 415-425, 26 dec. 2023. American Chemical Society (ACS).

89 TANG, W.; CAMERON, D. Aluminum-doped zinc oxide transparent conductors deposited by the sol-gel process. **Thin Solid Films**, [S.L.], v. 238, n. 1, p. 83-87, jan. 1994.

90 MARAGLIANO, C.; GLIA, A.; STEFANCICH, M.; CHIESA, M. Quantifying electrostatic force contributions in electrically biased nanoscale interactions. **J. Appl. Phys.**, [S.L.], v. 115, n. 12, 27 mar. 2014. Available at: AIP Publishing. http://dx.doi.org/10.1063/1.4869663. Accessed at: 10 dec. 2023.

91 ANAND, Y.. Microwave Schottky Barrier Diodes. **Metal-Semiconductor Schottky Barrier Junctions And Their Applications**, [S.L.], p. 219-271, 1984. Springer US.

92 KIM, H.; JUNG, M. J.; LEE, M. H.; CHOI, B. J. ALD growth of ZnO on GaN: Schottky barrier height engineering using ZnO interlayer. **Mater. Today Commun.**, [S.L.], v. 33, p. 104434, dec. 2022. Elsevier BV. Available at:http://dx.doi.org/10.1016/j.mtcomm.2022.104434. Accessed at: 18 dec. 2023.

93 GHENO, S. M.; KIMINAMI, R. H. G. A.; MORELLI, M. R.; Paulin Filho, P. I. Electric force microscopy investigations of barrier formations in ZnO-based varistors. **J. Eur. Ceram. Soc.**, [S.L.], v. 30, n. 2, p. 549-554, jan. 2010. Elsevier BV.